

Residual viscosity stabilized RBF-FD methods for solving nonlinear conservation laws

Igor Tominec^a, Murtazo Nazarov^b

^a*Uppsala University, Department of Information Technology, Division of Scientific Computing*

^b*Uppsala University, Department of Information Technology, Division of Scientific Computing*

Abstract

We formulate an oversampled radial basis function generated finite difference (RBF-FD) method to solve time-dependent nonlinear conservation laws. The analytic solutions of these problems are known to be discontinuous, which leads to occurrence of non-physical oscillations (Gibbs phenomenon) that pollute the numerical solutions and can make them unstable. We address these difficulties using a residual based artificial viscosity stabilization, where the residual of the conservation law indicates the approximate location of the shocks. The location is then used to locally apply an upwind viscosity term, which stabilizes the Gibbs phenomenon and does not smear the solution away from the shocks. The proposed method is numerically tested and proves to be robust and accurate when solving scalar conservation laws and systems of conservation laws, such as compressible Euler equations.

Keywords: nonlinear conservation law, stabilization, radial basis function, finite difference, oversampling, residual viscosity

1. Introduction

Radial basis function generated finite difference (RBF-FD) method for solving PDEs is a generalization of the classical finite difference method to scattered nodes. In this work we use an RBF-FD method to solve a nonlinear conservation law in the conservative form:

$$\partial_t \mathbf{U} = -\nabla \cdot \mathbf{F}(\mathbf{U}). \quad (1)$$

Here $\mathbf{U} = \mathbf{U}(y, t) \in \mathbb{R}^{k \times 1}$ is a solution vector of k functions, defined over an open and bounded domain $\Omega \subset \mathbb{R}^2$, where $y = (y_1, y_2) \in \bar{\Omega}$ is a spatial position and $t \in [0, T]$ is a position in time, where $T > 0$ is the final simulation time. We have that:

$$\mathbf{F}(\mathbf{U}) = [F_1(\mathbf{U}), F_2(\mathbf{U})]^T, \quad \mathbf{F}'(\mathbf{U}) = \frac{\partial \mathbf{F}(\mathbf{U})}{\partial \mathbf{U}}, \quad (2)$$

where $\mathbf{F}(\mathbf{U}) \in C^1(\mathbb{R}^k, \mathbb{R}^2)$ is a flux term, and $\mathbf{F}'(\mathbf{U})$ is denoted as the Jacobian matrix when $k > 1$ or the velocity field when $k = 1$. In this paper we focus on both, scalar conservation laws ($k = 1$) and systems of conservation laws ($k > 1$).

Since $\mathbf{F}(\mathbf{U})$ is nonlinear in \mathbf{U} , the analytic solutions of (1) with appropriate boundary conditions are discontinuous as $t \rightarrow \infty$, even if the initial condition is smooth. The points of discontinuities are referred to as *shocks*. The occurrence of shocks is problematic when they are numerically approximated, as it is known that the approximations in this case contain oscillations, see Figure 1. In order to avoid the oscillations which gradually evolve into instabilities while advancing the numerical solution in time, it is important to filter these oscillations out.

Email addresses: igor.tominec@it.uu.se (Igor Tominec), murtazo.nazarov@it.uu.se (Murtazo Nazarov)

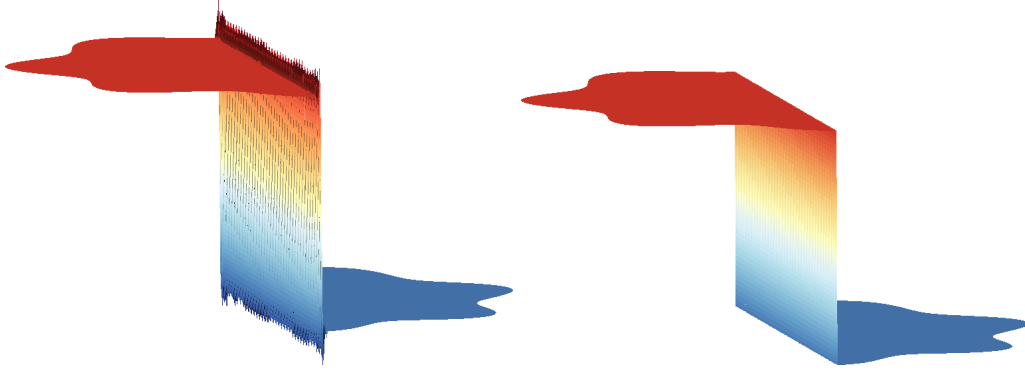


Figure 1: A discontinuous function drawn over a star shaped domain. Left: a numerical approximation exhibiting oscillations (Gibbs phenomenon). Right: the exact function without oscillations.

1.1. Radial basis function generated finite difference methods

In this paper we define and use an oversampled RBF-FD method for time-dependent PDEs, where an explicit time stepping method is used to advance the solution in time. The discretization is constructed using a sequence of local interpolation problems on stencils, such that the differential operators become rectangular matrices. The matrices then form a rectangular system of equations, which is reformulated to a square system of equations by using an appropriate projection technique. A similar formulation for time-dependent problems was in the context of a global RBF method made in [1]. The more standard, collocation RBF-FD methods [2, 3, 4, 5, 6, 7] are different to the oversampled RBF-FD methods in the sense that the differential operators are discretized such that the resulting system of equations is square by construction. The motivation to formulate an oversampled RBF-FD method for time-dependent problems stems from a study of an oversampled RBF-FD method with a least-squares projection for an elliptic model problem [8], where we found benefits compared with the collocation RBF-FD method in terms of stability and approximation error.

A standard way of stabilizing hyperbolic time-dependent problems within the RBF community is to augment the collocation scheme using a hyperviscosity term that damps high-frequency oscillations [9, 10, 11, 12], and makes the scheme stable in time. However, the hyperviscosity stabilization is ineffective in the presence of shocks, as is shown later in this paper, for example in Section 6, and then an additional type of stabilization has to be included to treat the shocks.

1.2. Stabilization of RBF-FD methods using a residual-based artificial viscosity term

A famous approach to control the Gibbs phenomenon and also other types of spurious oscillations, was introduced in the 1950s by von Neumann and Richtmyer [13]. The authors expanded a numerical discretization using a vanishing upwind viscosity term (also called a first-order viscosity term), which diffuses the oscillations, and give a so-called viscous solution. The solution is diffused throughout the whole computational domain, and not only in the regions with oscillations (shock formations). This can over diffuse the solution in general, including many interesting waves such as a contact discontinuity and a rarefaction, which would remain unresolved.

To avoid an excessive smearing of the solution, we localize the action of the viscosity term to regions with shocks. We formulate a residual based viscosity stabilization (RV) for the collocation and the oversampled RBF-FD methods. RV is mainly used within the finite element community. Its parent is the streamline diffusion (SD) method supplemented with an artificial viscosity term to form the SD+RV method [14], where the viscosity coefficient is determined from the residual of the PDE and has a shock capturing feature. The SD+RV method is difficult to implement and requires a coupled space-time discretization. To make a simplification, the SD terms were removed by Nazarov in [15], who only kept the RV term, and observed sufficient localized stabilization effects. In the same paper [15], Nazarov proved convergence of the RV stabilized finite element discretization that employs an implicit time stepping algorithm to advance the solution in time.

The RV stabilization is related to the well known entropy viscosity method of Guermond et al. [16], since the solution of a scalar conservation law can be one of the entropy functionals, however, this is not the case for the system of conservation laws. The RV method has also been used for stabilizing systems of conservation laws and discretizations other than the classical finite element methods in [17, 18, 19, 20],

The objective of the RV stabilization is to detect the position where the shock starts to form, by means of the magnitude of the numerical residual in (1). In the regions of Ω where the numerical solution starts to produce an overshoot over a shock, the residual is expected to be large, whereas in the regions where the solution is free of oscillations, the residual is expected to be small. The residual is then used as a weight for first-order viscosity term, which is included in the discretization. As a consequence, the weighted viscosity term is large only in the regions with shocks and potentially leads to a better approximation error.

1.3. Other stabilization techniques

A family of essentially non-oscillatory (ENO) methods introduced in [21] are based on grid discretization of a PDE and stabilize the Gibbs phenomenon by using a reconstruction step based on interpolation with the least oscillatory stencil. Weighted ENO (WENO) methods introduced in [22] use a convex combination of the candidate interpolation stencils to reconstruct a non-oscillatory function. There exist many subsequent papers on (W)ENO methods, see e.g., [23, 24, 25], where the authors develop (W)ENO methods using the RBF interpolants and by that allow approximations on unstructured grids.

Another class of stabilization methods are flux/slope limiters: these methods limit the derivatives of the solution to physically relevant magnitudes, see e.g., [26, 27, 28]. Employing limiters on unstructured grids is a non-trivial task.

1.4. Outline of the paper

In Section 2 we formulate an oversampled RBF-FD method for solving a scalar conservation law, and the Euler system of equations that models compressed gas dynamics. In Section 3 we derive a residual viscosity stabilization in the context of the RBF-FD method, for scalar conservation laws and Euler's system of PDEs. In Section 4 we make a comparison between the oversampled and the collocation RBF-FD methods when solving a linear conservation law (linear advection problem), and also numerically verify the consistency of the RV stabilization. In Section 5 and Section 6 we present numerical results for solving Burger's and the Kurganov-Petrova-Popov equations respectively. In Section 7 we solve several benchmark problems for the Euler equations. Final remarks are given in Section 8.

2. The oversampled RBF-FD discretization

In this section we describe the oversampled RBF-FD discretization that we use to solve (1). In particular, we describe our choice of point sets spread over Ω , the formation of evaluation and differentiation matrices using the RBF-FD method, and the discretization of a time-dependent PDE where an explicit method is used to advance the solution in time.

2.1. Point sets

The domain Ω is discretized using two point sets:

- the interpolation point set $X = \{x_i\}_{i=1}^N$ for generating the cardinal functions (left plot in Figure 2),
- the evaluation point set $Y = \{y_j\}_{j=1}^M$ for sampling the PDE (1) (right plot in Figure 2).

In the present work, we generate the X point set such that the mean distance between the points is set to a given value h . Depending on the application, the algorithms which we use are the 2D node generator from [29], Gmsh [30] or DistMesh [31]. The Y point set is generated by placing q points in each Voronoi region centered around every $x_i \in X$, $i = 1, \dots, N$, so that the relation between the number of X and Y points is $M \approx \lceil qN \rceil$, where we define q as the oversampling parameter.

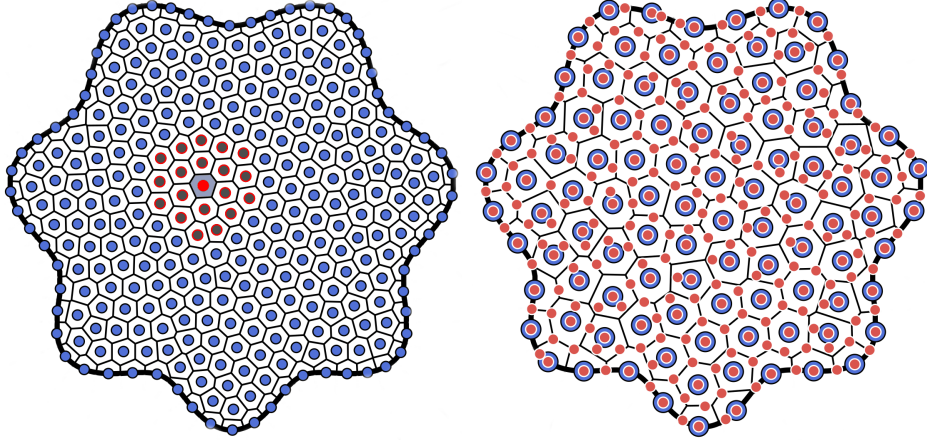


Figure 2: Left: an example of X points (blue points with black edges) that discretize the computational domain Ω , together with one stencil (black points with a red edge) centered around the point filled with a red color. Right: an example of Y points (small red points) added on top of X points, together with a Voronoi diagram, where each cell is centered around a corresponding X point.

2.2. Evaluation and differentiation matrices

We use the RBF-FD method in order to generate the RBF-FD trial space, which is spanned by a set of compactly supported cardinal basis functions $\{\Psi_i(y)\}_{i=1}^N$. These functions are constructed through a sequence of interpolation problems over stencils. An example of a stencil over Ω is given in Figure 2.

The cardinal basis functions are used to compute a PDE solution $u_h(Y, t)$ and a derivative $\mathcal{L}u_h(Y, t)$, in the form:

$$u_h(y, t) = \sum_{i=1}^N u_h(x_i, t) \Psi_i(y), \quad \mathcal{L}u_h(Y, t) = \sum_{i=1}^N u_h(x_i, t) \mathcal{L}\Psi_i(y), \quad (3)$$

where \mathcal{L} is a linear differential operator and $\{u_h(x_i, t)\}_{i=1}^N$ are the solution nodal values which are the unknowns.

Using $X = \{x_i\}_{i=1}^N$, we reformulate the relations in (3) using a semi-discrete matrix notation:

$$u_h(y, t) = E(y, X)u_h(X, t), \quad u_h^{\mathcal{L}}(y, t) = D^{\mathcal{L}}(y, X)u_h(X, t). \quad (4)$$

Here $u_h(X, t) = [u_h(X_1, t), \dots, u_h(X_N, t)]$ is the vector of nodal values and $E(y, X) = [\Psi_1(y), \dots, \Psi_N(y)]$, $D^{\mathcal{L}}(y, X) = [\mathcal{L}\Psi_1(y), \dots, \mathcal{L}\Psi_N(y)]$ are semi-discrete matrices constructed upon the RBF-FD evaluation/differentiation weights, where each set of weights is generated specifically for a point y . An algorithmic discussion on how to generate the evaluation and differentiation weights is given in [32]. A mathematical formulation for computing these weights is given in [33, 8]. In this paper we use these approaches to generate a vector of weights for every $y \in Y$, such that the weights are exact for a cubic polyharmonic spline basis and a monomial basis of degree p , which is a concept introduced in [34] and studied in [35, 36, 37, 38]. In our computations we use the stencil size $n = 2\binom{p+2}{2}$ for $p \geq 2$, and $n = 15$ for $p = 1$. To form evaluation and differentiation matrices, we sample (4) in each $y_k \in Y$, $k = 1, \dots, M$. This gives the following two relations:

$$u_h(Y, t) = E(Y, X)u_h(X, t), \quad u_h^{\mathcal{L}}(Y, t) = D^{\mathcal{L}}(Y, X)u_h(X, t), \quad (5)$$

where $E(Y, X)$ is a rectangular evaluation matrix of size $M \times N$ and $D^{\mathcal{L}}(Y, X)$ is a rectangular differentiation matrix of size $M \times N$. The two matrices can easily be computed in MATLAB by using the code provided in [39].

2.3. Discretization of a conservation law

Here we discretize (1), where we have k unknown functions that form a set $\mathbf{U} = (u_1, u_2, \dots, u_k)$. Each unknown function in \mathbf{U} is represented using the RBF-FD ansatz (3) such that:

$$\sum_{i=1}^N \partial_t \mathbf{U}_h(x_i, t) \Psi_i(y) = - \sum_{i=1}^N F_1(\mathbf{U}_h(x_i, t)) \nabla_1 \Psi_i(y) - \sum_{i=1}^N F_2(\mathbf{U}_h(x_i, t)) \nabla_2 \Psi_i(y),$$

where $\mathbf{U}_h(x_i, t) = (u_{h,1}(x_i, t), \dots, u_{h,k}(x_i, t))$ are the i -th unknown nodal values of the functions that we are solving the conservation law for, and where we used an interpolant of the flux $\mathbf{F}_l(\mathbf{U}_h(y, t)) = \sum_{i=1}^N \mathbf{F}_l(\mathbf{U}_h(x_i, t)) \Psi_i(y)$, $l = 1, 2$, to compute the divergence term in (1). Now we sample the equation above in every $y \in Y$ in order to obtain a system of M equations with N unknowns:

$$\begin{aligned} \sum_{i=1}^N \partial_t \mathbf{U}_h(x_i, t) \Psi_i(y_1) &= - \sum_{i=1}^N F_1(\mathbf{U}_h(x_i, t)) \nabla_1 \Psi_i(y_1) - \sum_{i=1}^N F_2(\mathbf{U}_h(x_i, t)) \nabla_2 \Psi_i(y_1) \\ &\vdots \\ \sum_{i=1}^N \partial_t \mathbf{U}_h(x_i, t) \Psi_i(y_M) &= - \sum_{i=1}^N F_1(\mathbf{U}_h(x_i, t)) \nabla_1 \Psi_i(y_M) - \sum_{i=1}^N F_2(\mathbf{U}_h(x_i, t)) \nabla_2 \Psi_i(y_M). \end{aligned} \quad (6)$$

The matrix-vector formulations for the two problems that we consider in this paper are collected in the subsections below.

2.4. Scalar conservation law in matrix-vector format

Discussion in this section is kept general in the sense that it applies to \mathbf{F} for scalar conservation laws. In this case we have that $\mathbf{U}_h = u_h$ and $\mathbf{F}(u_h) = [F_1(u_h), F_2(u_h)]$. Below, we rewrite the system (6) using the matrices defined in (5) and (4):

$$E(Y, X) \partial_t u_h(X, t) = -D^{\nabla_1}(Y, X) F_1(u_h(X, t)) - D^{\nabla_2}(Y, X) F_2(u_h(X, t)). \quad (7)$$

Here $E(Y, X)$, $D^{\nabla_1}(Y, X)$ and $D^{\nabla_2}(Y, X)$ are the rectangular evaluation and differentiation matrices of size $M \times N$ defined in Section 2.2. The vectors F_1 and F_2 of size $M \times 1$ correspond to the components of the (non)linear flux, thus their elements are $F_{1,i}(u_h(X, t)) = F_1(u_h(x_i, t))$ and $F_{2,i}(u_h(X, t)) = F_2(u_h(x_i, t))$ respectively. Now we multiply (7) with h_y , the approximate mean distance between the Y points to arrive at:

$$\bar{E}(Y, X) \partial_t u_h(X, t) = -\bar{D}^{\nabla_1}(Y, X) F_1(u_h(X, t)) - \bar{D}^{\nabla_2}(Y, X) F_2(u_h(X, t)). \quad (8)$$

where $\bar{E}(Y, X) = h_y E(Y, X)$ and $\bar{D}(Y, X) = h_y D(Y, X)$. The multiplication by h_y is a norm scaling introduced in [8], which makes it possible to couple our discrete problem to an equivalent continuous problem [8].

The rectangular system of equations (8) can not be solved using an explicit time-stepping technique in the form it has, as the system is rectangular and the time derivative on the left hand side is not explicitly defined. For this reason we project the residual of (8) onto the column space of $\bar{E}(Y, X)$ by multiplication with $\bar{E}^T(Y, X)$, where for simplicity, we also drop the (Y, X) notation and obtain:

$$\bar{E}^T \bar{E} \partial_t u_h(X, t) = \bar{E}^T (-\bar{D}^{\nabla_1} F_1(u_h(X, t)) - \bar{D}^{\nabla_2} F_2(u_h(X, t))). \quad (9)$$

Looking at (9), the components of the left hand side matrix $\bar{E}^T \bar{E}$ are:

$$(\bar{E}^T \bar{E})_{ij} = h_y^2 \sum_{k=1}^M \Psi_i(y_k) \Psi_j(y_k). \quad (10)$$

In other words, every component of $\bar{E}^T \bar{E}$ is a discrete inner product $(\Psi_i(y_k), \Psi_j(y_k))$, implying that $\bar{E}^T \bar{E}$ is a mass matrix in this inner product. The same type of inner product also applies to

the components of the right-hand-side matrix products. Thus, our projection using \bar{E}^T has a tight connection with a classical Galerkin projection. A key difference is that our type of discretization uses discrete (summation) instead of a continuous (exact integration) inner product.

Now we solve (9) for the time derivative $\partial_t u_h(X, t)$ by inverting the mass matrix $\mathcal{M} = \bar{E}^T \bar{E}$, in order to get a system of ODEs ready to be advanced in time:

$$\begin{aligned} \partial_t u_h(X, t) &= \mathcal{M}^{-1} \bar{E}^T (-\bar{D}^{\nabla_1} F_1(u_h(X, t)) - \bar{D}^{\nabla_2} F_2(u_h(X, t))) \\ &\equiv \mathcal{M}^{-1} \bar{E}^T \bar{D}(F(u_h(X, t))). \end{aligned} \quad (11)$$

Instead of directly inverting \mathcal{M} , we solve the system for $\partial_t u_h(X, t)$ iteratively, using the conjugate gradient method (function `pcg()` in MATLAB).

To (11) we also add two stabilization terms; (i) the term P_1 to stabilize the system of ODEs in time using a hyperviscosity operator, (ii) the term P_2 to treat the discontinuities which appear when using a nonlinear flux $\mathbf{F}(u_h)$. The scheme is then:

$$\partial_t u_h(X, t) = \mathcal{M}^{-1} \left[\bar{E}^T \bar{D}(F(u_h(X, t))) + P_1 u(X, t) + P_2 u(X, t) \right]. \quad (12)$$

This is a discretization of the scalar conservation law in conservative form. In this work we formulate the hyperviscosity term $P_1 \approx \Delta^2$ as:

$$\begin{aligned} P_1 &= \gamma h_y^2 [D^{\Delta_{11}}(Y, X) + D^{\Delta_{22}}(Y, X)]^T [D^{\Delta_{11}}(Y, X) + D^{\Delta_{22}}(Y, X)] \\ \gamma &= h^{4.5}, \end{aligned} \quad (13)$$

where h_y^2 is the norm scaling and γ is the hyperviscosity scaling. Our choice of γ is justified by making the γP_1 term consistent with the PDE up to the 4-th order, and then increasing that number to 4.5 in order to allow a larger time step when using an explicit time-stepping algorithm. Term P_2 is constructed using the residual viscosity concept described in Section 3.

Note that when the flux $\mathbf{F}(u_h)$ is linear, then the conservative and the non-conservative forms of a conservation laws exhibit the same numerical properties, and the ODE system (12) transforms to:

$$\partial_t u_h(X, t) = \mathcal{M}^{-1} \bar{E}^T (-F'_1 \bar{D}^{\nabla_1} - F'_2 \bar{D}^{\nabla_2}) u_h(X, t) - (P_1 + P_2) u_h(X, t) \equiv \bar{D} u_h(X, t). \quad (14)$$

Here F'_1 and F'_2 correspond to the components of the velocity field $\mathbf{F}'(t)$. More specifically, they represent rectangular identity matrices of size $M \times N$ with components $F'_{1,ii} = F'_1(t)$, $F'_{2,ii} = F'_2(t)$, $i = 1, \dots, N$.

At this point we can use an explicit time-stepping algorithm to advance the solution of (12) from $t = 0$ to $t = T$. Throughout this paper we use an explicit classical Runge-Kutta 4 time-stepping algorithm. In the numerical experiment section of the paper we solve problems with Dirichlet-type boundary conditions on the inflow boundary. To impose these conditions we use a so-called injection method, that is, we step the discretization (12) and then in every time step overwrite the correct subset of boundary elements of $u_h(X, t)$ with the corresponding values of the Dirichlet boundary condition. After the nodal solution $u(X, T)$ at the final time $t = T$ is obtained, we evaluate the solution at Y points as:

$$u_h(Y, T) = E(Y, X) u_h(X, T). \quad (15)$$

2.5. System of conservation laws in matrix-vector format: compressible Euler equations

Consider compressible Euler equations in two spatial dimensions. The unknowns \mathbf{U} and the flux $\mathbf{F}(\mathbf{U})$ are in this case given by:

$$\mathbf{U} = \begin{pmatrix} \rho \\ \mathbf{m} \\ \mathcal{E} \end{pmatrix}, \quad \mathbf{F}(\mathbf{U}) = \begin{pmatrix} \mathbf{m} \\ \mathbf{m} \otimes \mathbf{v} + p \mathbf{I} \\ \mathbf{v}(\mathcal{E} + p) \end{pmatrix}. \quad (16)$$

Here \mathbf{I} is an identity matrix, ρ is the density, $\mathbf{m} = (m_1, m_2)$ is the momentum, \mathcal{E} is the total energy and p is the pressure of the fluid. The relation between the momentum and the velocity field is

$\mathbf{v} = \mathbf{m}/\rho$. When forming a system of equations we have 5 unknown functions, but only 4 equations. We close the system of equations using an ideal gas condition, by defining the pressure variable as: $p = \rho T = (c_{\text{ad}} - 1)(\mathcal{E} - \rho|\mathbf{v}|^2/2)$, where T is the temperature of the fluid and c_{ad} is the adiabatic gas constant. In this case the expanded form of the nonlinear conservation law (1) is:

$$\partial_t \begin{pmatrix} \rho \\ m_1 \\ m_2 \\ \mathcal{E} \end{pmatrix} = \begin{pmatrix} -\nabla_1 m_1 - \nabla_2 m_2 \\ -\nabla_1(m_1 v_1) - \nabla_2(m_2 v_1) - \nabla_1 p \\ -\nabla_1(m_1 v_2) - \nabla_2(m_2 v_2) - \nabla_2 p \\ -\nabla_1(v_1(\mathcal{E} + p)) - \nabla_2(v_2(\mathcal{E} + p)) \end{pmatrix} \quad (17)$$

We discretize the above system by introducing unknown nodal values for all unknown functions $\rho(X, t), m_1(X, t), m_2(X, t), \mathcal{E}(X, t)$. The oversampled RBF-FD discretization analogous to (12) is then:

$$\partial_t \begin{pmatrix} \rho(X, t) \\ m_1(X, t) \\ m_2(X, t) \\ \mathcal{E}(X, t) \end{pmatrix} = \mathcal{M}^{-1} \begin{pmatrix} E^T G_\rho(Y, t) + P\rho(X, t) \\ E^T G_{m_1}(Y, t) + Pm_1(X, t) \\ E^T G_{m_2}(Y, t) + Pm_2(X, t) \\ E^T G_\mathcal{E}(Y, t) + P\mathcal{E}(X, t) \end{pmatrix} \quad (18)$$

where:

$$\begin{aligned} G_\rho(Y, t) &= -D^{\nabla_1} m_1(X, t) - D^{\nabla_2} m_2(X, t) \\ G_{m_1}(Y, t) &= -D^{\nabla_1}(m_1(X, t) v_1(X, t)) - D^{\nabla_2}(m_2(X, t) v_1(X, t)) - D^{\nabla_1} p \\ G_{m_2}(Y, t) &= -D^{\nabla_1}(m_1(X, t) v_2(X, t)) - D^{\nabla_2}(m_2(X, t) v_2(X, t)) - D^{\nabla_2} p \\ G_\mathcal{E}(Y, t) &= -D^{\nabla_1}(v_1(\mathcal{E} + p)) - D^{\nabla_2}(v_2(\mathcal{E} + p)) \\ P &= -P_1 - P_2, \end{aligned} \quad (19)$$

with differentiation matrices $D^{\nabla_1}, D^{\nabla_2}$ defined in Section 2.2, and stabilizers P_1 and P_2 described in Section 2.4. The Dirichlet-type boundary conditions for a given unknown function are imposed using the injection method, just as described for the scalar conservation law in Section 2.4. After the system of ODEs is advanced to the final time $t = T$, each unknown set of nodal values is evaluated at the Y points, analogously to (15).

3. Residual based artificial viscosity stabilization of shocks for nonlinear conservation laws

Solutions to nonlinear conservation laws (1) are discontinuous, when the flux $\mathbf{F}(\mathbf{U})$ does not include any physical viscous forces. Numerical approximation of discontinuous functions suffers from the Gibbs phenomenon. Based on [15, 17, 40] we formulate a residual based viscosity stabilization of the solution in the context of the RBF-FD method.

The numerical scheme is stabilized using a viscosity term $P_2 \approx \nabla \cdot (\varepsilon \nabla u)$, where ε is a spatially variable coefficient, computed such that the viscous term is prevalently active in the regions of discontinuities. The viscosity term is below discretized by using the differentiation matrices introduced in Section 2.2:

$$P_2 = (D^{\nabla_1})^T \text{diag}(E \varepsilon(X, t_n)) D^{\nabla_1} + (D^{\nabla_2})^T \text{diag}(E \varepsilon(X, t_n)) D^{\nabla_2}. \quad (20)$$

The definition of ε for scalar conservation laws and the Euler system, is given in the following two subsections.

3.1. Definition of the viscosity coefficient for scalar conservation laws

The discrete problem which we aim to stabilize is (12). The discussion is centered around the stabilization term P_2 defined in (20). For each node $x_i \in X$, $i = 1, \dots, N$, we define the viscosity coefficient vector ε included inside the definition of P_2 as:

$$\begin{aligned} \varepsilon(x_i, t_{n+1}) &= \min(\varepsilon_{\text{RV}}(x_i, t_n), \varepsilon_{\text{UW}}(x_i, t_n)), \quad n = 2, 3, \dots \\ \varepsilon(x_i, t_{n+1}) &= \varepsilon_{\text{UW}}(x_i, t_n), \quad n = 1. \end{aligned} \quad (21)$$

Here ε_{RV} and ε_{UW} are the residual and the upwind coefficients respectively. Let K_i be a Voronoi cell with a corresponding Voronoi center x_i , and $y_j \in Y$ an evaluation point (see the right plot in Figure 2). Then the definitions of ε_{RV} and ε_{UW} are [15]:

$$\begin{aligned}\varepsilon_{\text{RV}}(x_i, t_{n+1}) &= C_{\text{RV}} h_{\text{loc}}^2(x_i) \max_{y_j \in K_i} |R(y_j, t_n)| \frac{1}{n(x_i)}, \\ \varepsilon_{\text{UW}}(x_i, t_{n+1}) &= \frac{1}{2} h_{\text{loc}}(x_i) \max_{y_j \in K_i} \sqrt{F_1'(u_h(y_j, t_n))^2 + F_2'(u_h(y_j, t_n))^2}.\end{aligned}\quad (22)$$

Here we define $h_{\text{loc}}(x_i)$ as the minimum pairwise distance between points in a patch centered around x_i , where the patch consists of 5 points closest to x_i [18]. The temporal solution $u_h(y_j, t_n)$ at a point $y_j \in Y$ comes from the relation $u_h(Y, t_n) = E(Y, X) u_h(X, t_n)$. The user-defined constant C_{RV} is of size $\mathcal{O}(1)$ and is independent of $h_{\text{loc}}(x_i)$. As $C_{\text{RV}} \rightarrow \infty$, then $\varepsilon_{\text{RV}} \rightarrow \infty$, and $\varepsilon \rightarrow \varepsilon_{\text{UW}}$. On the other hand, as $C_{\text{RV}} \rightarrow 0$, then $\varepsilon_{\text{RV}} \rightarrow 0$, and $\varepsilon \rightarrow 0$. The term $n(x_i, t_n)$ is the residual normalization defined by:

$$\begin{aligned}n(x_i, t_n) &= \left| u_{\text{loc}} - \|u_h(X, t_n) - \bar{u}_h(X, t_n)\|_\infty \right|, \\ u_{\text{loc}} &= \max_{y_j \in K_i} u_h(y_j, t_n) - \min_{y_j \in K_i} u_h(y_j, t_n),\end{aligned}\quad (23)$$

where $\bar{u}_h(X, t_n)$ is the mean of the temporal solution $u_h(X, t_n)$. The role of the normalization is to unify the physical units of ε_{RV} and ε_{UW} . The residual $R(Y, t_n)$ is defined as:

$$R(Y, t_n) = E(D^{\partial_t} u_h(X, t_n)) + D^{\nabla_1} F_1(u_h(X, t_n)) + D^{\nabla_2} F_2(u_h(X, t_n)), \quad (24)$$

where $D^{\nabla_1} F_1(u_h(X, t_n)) + D^{\nabla_2} F_2(u_h(X, t_n))$ is the flux divergence of the solution at time t_n computed using the RBF-FD differentiation matrices introduced in Section 2.2. Furthermore, E is an evaluation matrix also introduced in Section 2.2, and the term $D^{\partial_t} u_h(X, t_n)$ is an approximation of the time derivative at t_n using the already computed solution from previous time points $t_n, t_{n-1}, t_{n-2}, \dots$. We construct D^{∂_t} in two different ways: (i) when the solution is advanced in time using a constant Δt we use the backward-differentiation formulae (BDF), (ii) when the solution is advanced in time by a variable Δt_i , $i = 1, 2, \dots$, then we construct an approximation to a time derivative using the polynomial basis, in each time step. In any case, the approximation order in (i) or (ii) has to match the approximation order of the spatial discretization. At the beginning of the simulation we can only use a few points from the past temporal solutions. When a sufficient amount of temporal solutions have been computed we are allowed to use a high-order formula. We then write that:

$$D^{\partial_t} \Big|_{t_n} = \begin{cases} D_1^{\partial_t} & n = 2 \\ D_2^{\partial_t} & n = 3 \\ D_3^{\partial_t} & n = 4 \\ D_4^{\partial_t} & n \geq 5, \end{cases} \quad (25)$$

where $D_1^{\partial_t}$ is a differentiation operator of order 1, $D_2^{\partial_t}$ of order two, and so on. In the case (i) we use the BDF4 formula to define $D_k^{\partial_t}$, for $\bar{k} = 1, \dots, 4$ consecutively as:

$$\begin{aligned}& \frac{1}{\Delta t} (U(X, t_n) - U(X, t_{n-1})), \\ & \frac{1}{\Delta t} \frac{3}{2} \left(U(X, t_n) - \frac{4}{3} U(X, t_{n-1}) + \frac{1}{3} U(X, t_{n-2}) \right), \\ & \frac{1}{\Delta t} \frac{11}{6} \left(U(X, t_n) - \frac{18}{11} U(X, t_{n-1}) + \frac{9}{11} U(X, t_{n-2}) - \frac{2}{11} U(X, t_{n-3}) \right), \\ & \frac{1}{\Delta t} \frac{25}{12} \left(U(X, t_n) - \frac{48}{25} U(X, t_{n-1}) + \frac{36}{25} U(X, t_{n-2}) - \frac{16}{25} U(X, t_{n-3}) + \frac{3}{25} U(X, t_{n-4}) \right).\end{aligned}\quad (26)$$

In the case (ii) we construct $D_k^{\partial_t}$, $\bar{k} = 1, \dots, 4$ by computing a set of differentiation weights through a 1D polynomial interpolant $u(t) = \sum_{j=1}^{\bar{k}+1} \xi_j t^{j-1}$, where $\bar{k} + 1$ is the number of the time points

in which we already know the solution $u(t_1), u(t_2), \dots, u(t_{k+1})$, and \bar{k} is the desired order of the approximation. Then we sample $u(t)$ in $t_n, t_{n-1}, \dots, t_{n-q_t}$ to obtain a system of equations $\underline{u} = A \underline{\xi}$, where $A_{ij} = t_i^{j-1}$ and $\xi_i, j = 1, \dots, \bar{k} + 1, i = 1, \dots, \bar{k} + 1$ are the interpolation matrix and the unknown coefficients respectively. A time-derivative of $u(t)$ is $\partial_t u(t) = \sum_{j=1}^{\bar{k}+1} (j-1)t^{j-2} \xi_j$, an equivalent vector formulation is $\partial_t u(t) = \underline{b}(t) \underline{\xi}$, where $b_j(t) = (j-1)t^{j-2}$. Plugging the computed $\underline{\xi}$ into $\partial_t u(t)$ we have $\partial_t u(t) = \underline{b}(t) A^{-1} \underline{u} \equiv \underline{w}(t) \underline{u}$. Here $\underline{w}(t)$ is a final vector of $k+1$ weights for computing a derivative in time when the time grid is non-uniform. The MATLAB code to compute \underline{w} is provided in [Appendix A](#).

Note that the time derivative approximated using the approaches (i) and (ii), is used only with the purpose to compute the residual, once the solution at t_n has already been computed. The time stepping scheme that is actually advancing the solution in time is chosen differently.

3.2. Definition of the viscosity coefficient for the Euler system

Here we formulate the viscosity coefficient ε for the Euler system of equations (18). The ε coefficient is computed using the same relation as in (21), however, the definitions of ε_{UW} and ε_{RV} in (21) are different. The upwind viscosity coefficient at time t_{n+1} and a point $x_i \in X$ is defined as:

$$\varepsilon_{\text{UW}}(x_i, t_{n+1}) = \frac{1}{2} h_{\text{loc}}(x_i) \left(\sqrt{v_1^2(x_i, t_n) + v_2^2(x_i, t_n)} + \sqrt{c_{\text{ad}} T(x_i, t_n)} \right), \quad (27)$$

where the term in parenthesis is the local wave speed computed from the eigenvalues of $\frac{\partial \mathbf{F}}{\partial \mathbf{U}}$, and where $v_1(x_i, t_n) = m_1(x_i, t_n)/\rho(x_i, t_n)$, $v_2(x_i, t_n) = m_2(x_i, t_n)/\rho(x_i, t_n)$ are the velocities in horizontal and vertical directions respectively, and $T = p(x_i, t)/\rho(x_i, t)$ is the temperature of the fluid, and the internodal distance $h_{\text{loc}}(x_i)$ is defined in the scope of (22). The coefficient ε_{RV} is defined by:

$$\varepsilon_{\text{RV}} = C_{\text{RV}} h_{\text{loc}}^2(x_i) \max \left(\frac{|R_\rho|}{n_\rho}, \frac{|R_{m_1}|}{n_{m_1}}, \frac{|R_{m_2}|}{n_{m_2}}, \frac{|R_\mathcal{E}|}{n_\mathcal{E}} \right), \quad (28)$$

where the residuals R_* are defined for each equation in (18), analogously to the formulation for the scalar conservation law in (24). We have:

$$\begin{aligned} R_\rho(Y, t_n) &= E \left(D_{\text{BDF}}^{\partial_t} \rho(X, t_n) \right) - G_\rho(Y, t_n) \\ R_{m_1}(Y, t_n) &= E \left(D_{\text{BDF}}^{\partial_t} m_1(X, t_n) \right) - G_{m_1}(Y, t_n) \\ R_{m_2}(Y, t_n) &= E \left(D_{\text{BDF}}^{\partial_t} m_2(X, t_n) \right) - G_{m_2}(Y, t_n) \\ R_\mathcal{E}(Y, t_n) &= E \left(D_{\text{BDF}}^{\partial_t} \mathcal{E}(X, t_n) \right) - G_\mathcal{E}(Y, t_n). \end{aligned} \quad (29)$$

Here G_ρ, G_{m_1}, G_{m_2} and $G_\mathcal{E}$ are defined in (19), and the time derivative approximation $D_{\text{BDF}}^{\partial_t}$ is the same as defined in (25) and (26). Each normalization n_* in (28) follows the same definition as in (23). For example, n_ρ is defined as:

$$\begin{aligned} n_\rho(x_i, t_n) &= \left| \rho_{\text{loc}} - \|\rho(X, t_n) - \bar{\rho}(X, t_n)\|_\infty \right|, \\ \rho_{\text{loc}} &= \max_{y_j \in K_i} \rho(y_j, t_n) - \min_{y_j \in K_i} \rho(y_j, t_n), \quad i = 1, \dots, N \end{aligned} \quad (30)$$

where $\bar{\rho}(X, t_n)$ is the mean density at $t = t_n$ and K_i is a Voronoi cell centered around $x_i \in X$.

4. Numerical study I: linear advection problem

Throughout this section we compare collocation and oversampled RBF-FD methods, and investigate how do the hyperviscosity term (13) and the residual viscosity term (20) influence the numerical solution. Consider \mathbf{F} is a linear flux with time-dependent velocity field given by:

$$\mathbf{F}'(u) = \mathbf{F}' = (\cos(2\pi t), \sin(2\pi t)). \quad (31)$$

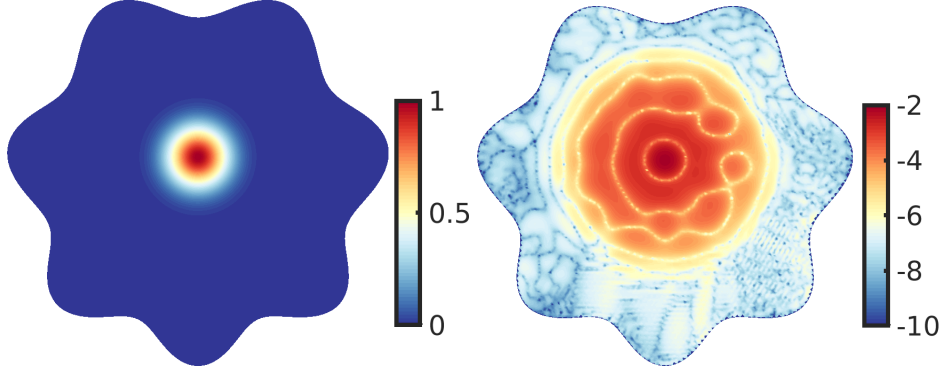


Figure 3: Linear advection of a compactly supported C^6 function using a rotational velocity field. Initial condition is given in the left image. The spatial error distribution in the \log_{10} scale, after the initial condition is rotated five times, and an oversampled RBF-FD method is in time stabilized using hyperviscosity, is given in the image on the right. Method parameters are set to $h = 0.03$ and $p = 4$ and $q = 5$.

The boundary of Ω is defined using polar coordinates (r, θ) , where: $r = 1 + \frac{1}{10}(\sin(7\theta) + \sin(\theta))$ for $\theta \in [0, 2\pi]$. We use the explicit classical Runge-Kutta 4 method to advance the solution in time. The constant time step is chosen as:

$$\Delta t = \text{CFL} \min_{x_i \in X} \frac{h_{\text{loc}}(x_i)}{\sqrt{(F'_1(t))^2 + (F'_2(t))^2}} = \text{CFL} \min_{x_i \in X} h_{\text{loc}}(x_i), \quad (32)$$

where we also used that $(F'_1(t))^2 + (F'_2(t))^2 = 1$, since \mathbf{F}' is in (31) chosen as the rotational velocity field. The term $h_{\text{loc}}(x_i)$ is defined in the scope of (22). The constant CFL is the Courant-Friedrichs-Lax number, specified in each subsection separately. The relative approximation errors in 2- and 1-norm at final time $t = T$ are computed as:

$$\|e\|_2 = \frac{\|E(Y, X) u_h(X, T) - u(Y, T)\|_2}{\|u(Y, T)\|_2}, \quad \|e\|_1 = \frac{\|E(Y, X) u_h(X, T) - u(Y, T)\|_1}{\|u(Y, T)\|_1}, \quad (33)$$

where $u(Y, T)$ is the exact solution at $t = T$, sampled at Y points.

4.1. Smooth initial condition: approximation error and stability properties

Oversampled methods are normally associated with improved stability properties. In this section we investigate whether this is also true when solving hyperbolic problems, i.e., if there is a positive effect of oversampling on the eigenvalue spectrum of the discretized advection operator.

Provided that $d = d(y_1, y_2) = \sqrt{(y_1 - 0.2)^2 + (y_2 - 0.2)^2}$, the initial condition at $t = 0$ is a C^6 compactly supported Wendland function centered in a point $(0.2, 0.2)$:

$$u(y, 0) = \begin{cases} (1 - d)^6 (35d^2 + 18d + 3), & d \leq 0.4 \\ 0, & \text{otherwise.} \end{cases} \quad (34)$$

The initial condition is plotted in Figure 3. The discretized advection operator D is given in (14). In this section we do not observe effects due to the stabilization of shock, therefore, we set $P_2 = 0$. When studying eigenvalues, we enforce zero Dirichlet boundary condition exactly in D , by removing all rows and columns corresponding to the boundary unknowns. In Figure 4 we display a close up of the eigenvalue spectrum around the imaginary axis, when the discretization is not stabilized, that is, when the parameter γ in P_1 included into (14) is set to 0. We observe that the spectrum of the collocation RBF-FD method includes eigenvalues with a positive real part. These eigenvalues cause spurious growth when the solution is advanced in time. However, the situation is not improved as we introduce an oversampled discretization: for the oversampling parameters $q = 5$, $q = 20$ and $q = 30$, the eigenvalue spectra still include eigenvalues with a positive real part. We do not observe that the positive real part is asymptotically shifted towards the negative imaginary half-plane, as q

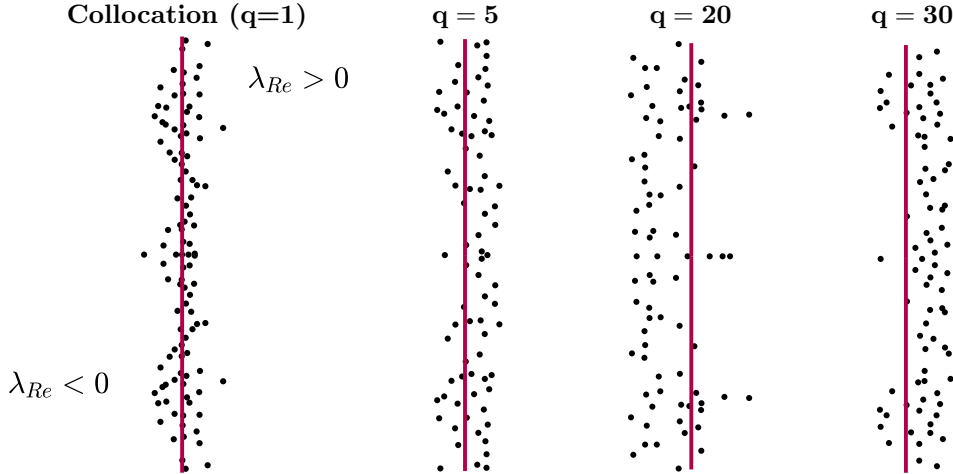


Figure 4: Linear advection of a compactly supported C^6 function using a rotational velocity field: a close-up of the eigenvalue spectra for different choices of the oversampling parameter q , when none of the cases is stabilized using hyperviscosity. Eigenvalues left of the red line have a negative real part, while the eigenvalues on the right of the red line have a positive real part.

is increased. Our conclusion is that oversampling by itself does not stabilize the eigenvalue spectrum of the semi-discrete PDE problem when the RBF-FD method is used.

Next, we study the eigenvalue spectra when hyperviscosity is added to (14), that is, when the parameter γ and the second-order hyperviscosity P_1 follow the definition in (13). The results are given in Figure 5, where we observe that the eigenvalue spectra are stabilized. The eigenvalue distributions are similar across the different methods.

Now we compare the hyperviscosity stabilized collocation and oversampled RBF-FD methods in terms of the approximation error when the internodal distance h is decreased ($1/h$ increased). The simulation is run until $t = 5$. In this time the initial condition makes five full rotations around the point $(0, 0)$. To determine the time step we use $CFL = 0.2$. Convergence results are collected in Figure 6. For all tested degrees of the appended monomial bases, we observe that the errors are very similar in magnitude and convergence trend, for both collocation and oversampled RBF-FD methods. An increase in the oversampling parameter does not lead to a better accuracy in this case. This conclusion is in line with the results on solving elliptic PDEs with pure Dirichlet boundary conditions, presented in [8]. An example of a spatial error distribution after five revolutions of the initial condition is displayed in Figure 3.

4.2. Smooth initial condition: a residual viscosity test

We again use (31) as the velocity field and a compactly supported C^6 Wendland function (34) as the initial condition. The difference compared with the previous experiment is that we now activate the residual viscosity (RV) term P_2 in our discretization (14). The objective is to check if P_2 distorts high-order convergence when the solution is smooth. We use $C_{RV} = 1$ as the scaling used in (22). We use $CFL = 0.5$ and run our simulation until $t = 1$. The results are collected in Figure 7. We observe that the approximation error is slightly larger throughout the refinement of h when RV is used. However, the convergence trend when RV is used does not change significantly compared with the case when RV is not used. This is accounted to the fact that the residual is small when no discontinuity is present in the numerical solution. Since the coefficient ε given in (21) that scales P_2 in (20) is residual dependent, the viscosity terms plays a negligible role in the numerical discretization given in (14). An important outcome of this subsection is that the residual viscosity can be used in cases when we do not know whether the solution is going to develop a shock, without sacrificing the order of convergence before the shock is developed.

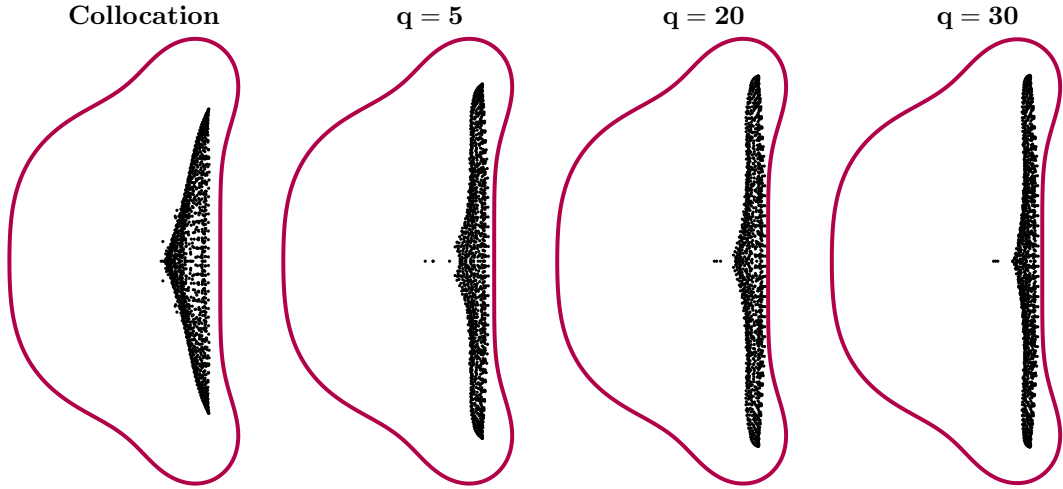


Figure 5: Linear advection of a compactly supported C^6 function using a rotational velocity field: eigenvalue spectra for different choices of the oversampling parameter q , when the discretizations are stabilized in time using the hyperviscosity term. The closed red line represents stability region of the Runge-Kutta 4 method for advancing the system of ODEs in time.

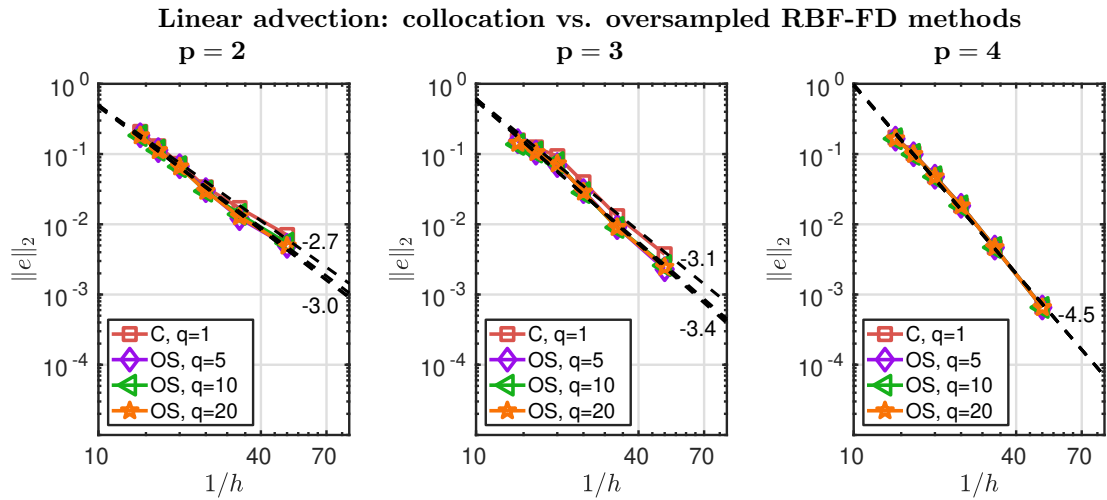


Figure 6: Linear advection of a compactly supported C^6 function using a rotational velocity field: convergence as a function of the inverse internodal distance $1/h$. Experiments in each plot correspond to using a different degree of monomial basis p used to construct the RBF-FD trial space. Within each plot, different oversampling parameters q are used to oversample (OS) the semi-discrete system of ODEs. The case $q = 1$ represents the collocation RBF-FD method, and other choices of q represent the oversampled RBF-FD method.

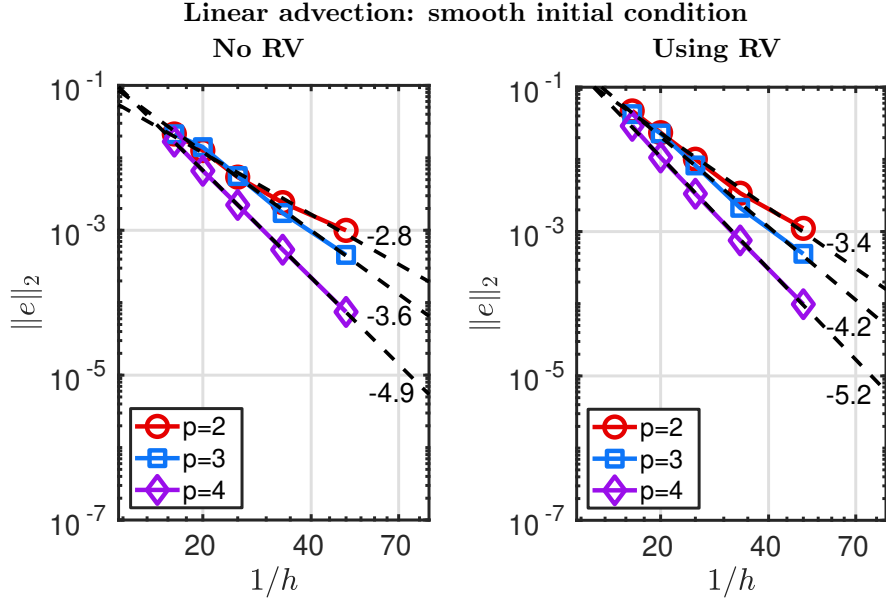


Figure 7: Linear advection of a compactly supported C^6 function using a rotational velocity field: convergence as a function of the inverse internodal distance $1/h$, for an oversampled RBF-FD method ($q = 5$). The CFL number is set to 0.2, the initial condition is rotated until time $t = 1$.

4.3. Discontinuous initial condition: a residual viscosity test

Now we again consider a linear advection problem with (31) as the velocity field, but use a discontinuous initial condition; a cylinder with radius 0.3, cut from two sides, given in Figure 8. We

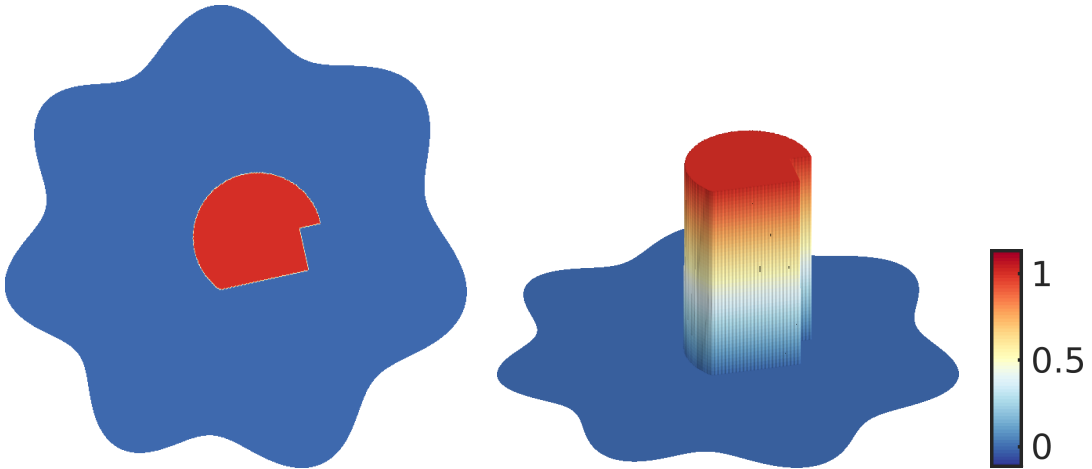


Figure 8: Linear advection of a discontinuous initial condition: exact solutions at $t = 1$, drawn from two perspectives.

let the initial condition rotate around its axis one time (until $t = 1$) when $h = 0.01$, $p = 4$, and compare three scenarios:

1. Residual viscosity is not active: in (20) we set $\varepsilon = 0$.
2. Only the first order viscosity is active: instead of following the definition of ε in (21) we set $\varepsilon = \varepsilon_{UV}$ throughout Ω .
3. Residual viscosity is active: ε is taken as defined in (21).

Note that the hyperviscosity term P_1 is essential to stabilize the discretization in time and is active in all three scenarios. We use $CFL = 0.1$ when using first-order viscosity and $CFL = 0.5$ when using RV and when not stabilizing discontinuities. We use $C_{RV} = 1$ as the scaling used in (22). Results for the collocation RBF-FD method and an oversampled RBF-FD method are given in Figure 9 (side view).

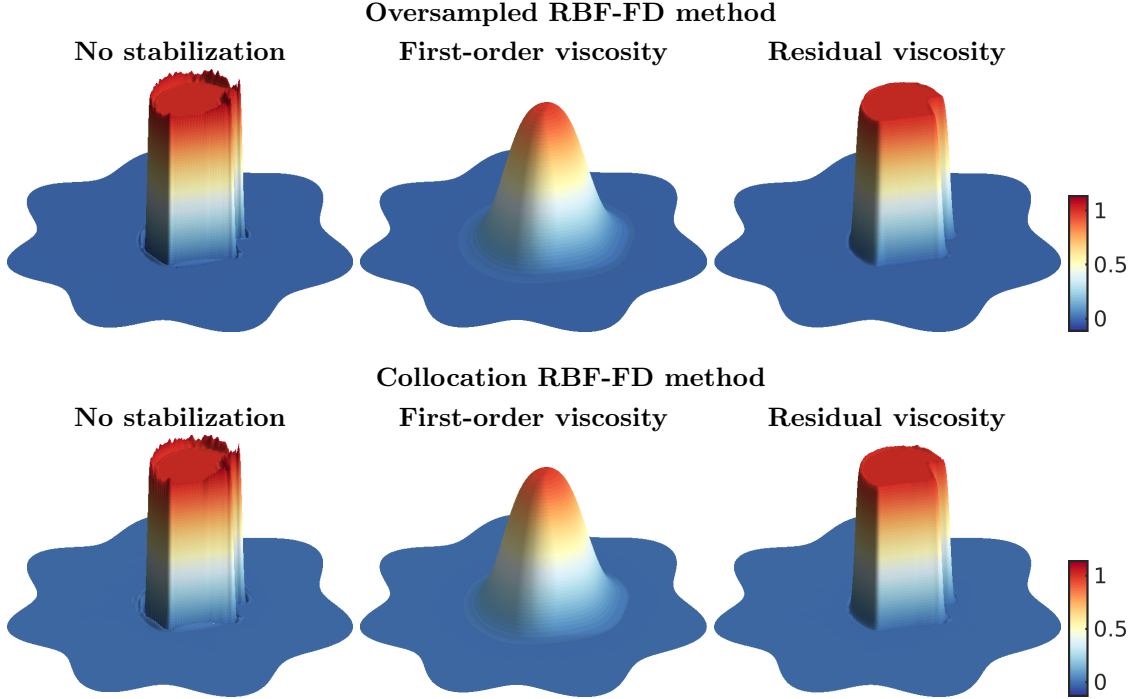


Figure 9: Linear advection of a discontinuous initial condition when different stabilization techniques are used, side view. All solutions are displayed after one rotation at $t = 1$. Parameters used were $h = 0.01$, $p = 4$, $q = 5$. The CFL condition when first-order viscosity was set to 0.1, and to 0.5 in cases when residual viscosity method was used and when no stabilization was used.

From the two figures we observe that the numerical scheme without stabilization induces oscillations (Gibbs phenomenon) around the discontinuity. This is expected. When the numerical scheme is stabilized by the first-order viscosity term, we observe that the initial condition is highly smeared, to the extent where it is difficult to recognize the characteristic shape of the initial condition. The main observation is that after the oversampled RBF-FD method is stabilized using the residual viscosity term, the oscillations are significantly damped, while the initial condition kept its characteristic shape throughout the simulation. We observe that the RV solution is not significantly different compared with the RV solution when an oversampled RBF-FD method is used. It is however possible to observe a few more oscillations on the outer edge of the slotted cylinder, when the collocation RBF-FD method is used.

The effectiveness of the residual viscosity method when an oversampled RBF-FD method is used, is displayed in Figure 10, where we show the spatial distribution of the residual (24) and the coefficient ε given in (21). We observe that the residual is giving the information about the position of the discontinuity (large oscillations) present in the solution. This makes the residual viscosity coefficient ε (defined in (21) and (22)) large in the region of the shock, but small away from the shock. The results for the oversampled and the collocation RBF-FD methods are – in the “eyeball norm” – identical. We conclude that for the cases considered in this subsection, the residual viscosity approach detects discontinuities in an accurate way, for both RBF-FD methods that we tested. In this paper we are mainly interested in the performance of the oversampled RBF-FD method, which we now focus on in the results below.

In Figure 11 we provide convergence results for the oversampled RBF-FD method, for different

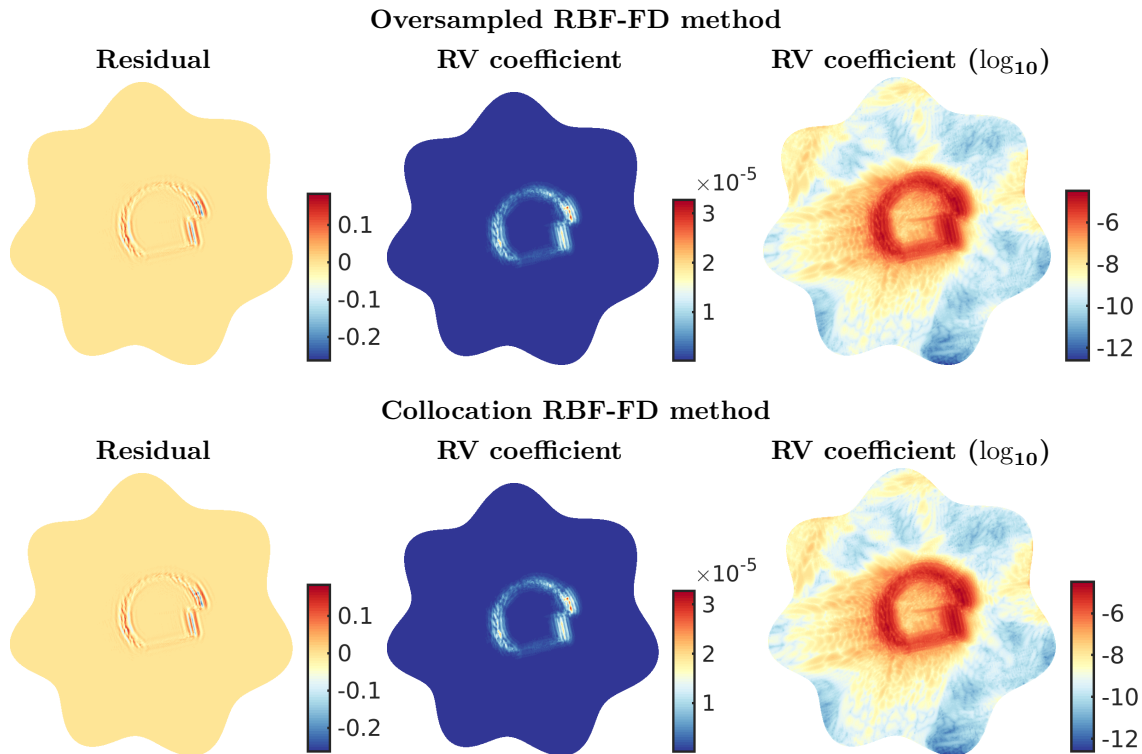


Figure 10: Linear advection of a discontinuous initial condition when residual viscosity is used. The pictures show the residual and the residual-viscosity (RV) coefficients in linear and logarithmic scale.

choices of p , when the numerical scheme includes: (i) no stabilization, (ii) first-order viscosity, (iii) residual-viscosity. The CFL numbers used for the simulation were 0.2 for cases (i) and (ii), and 0.1 for case (iii). The observed convergence rates in all cases are what we expect, since the solution is discontinuous and the error is measured in 2-norm. The approximation error is smallest in the case where no shock stabilization is added. This can be accounted to an observation made in Figure 9, where oscillations when no shock stabilization was added were not as severe as one expected. However, we do expect the oscillations to become significantly larger when the flux $\mathbf{F}(u)$ becomes nonlinear with respect to u (studied in later sections). Additional experiments revealed that the approximation error in ∞ -norm does not converge, which is expected.

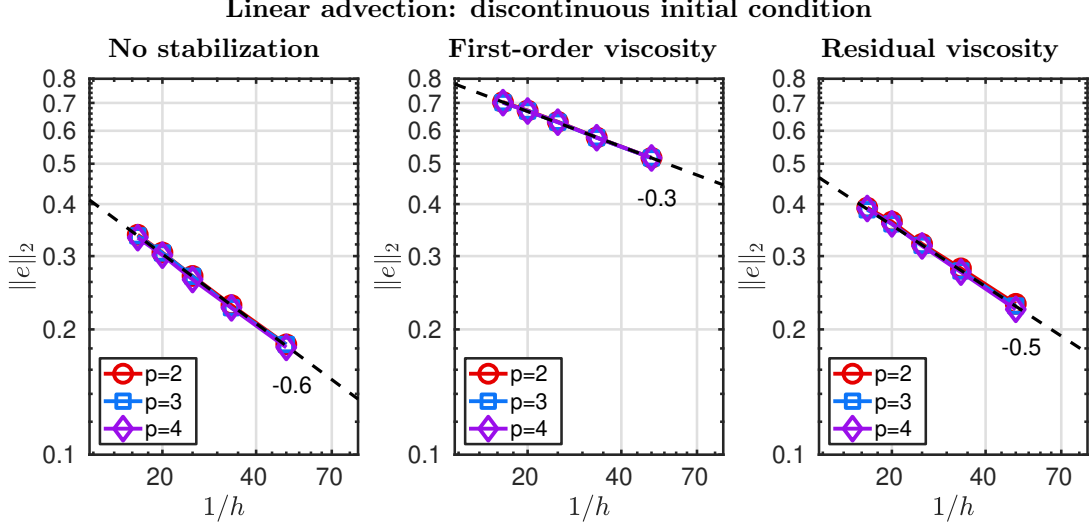


Figure 11: Linear advection of a discontinuous initial condition, convergence study of the approximation error under node refinement, for different degrees p of the monomial basis used to construct the interpolation problem over a stencil. The three plots show cases when numerical scheme includes: (i) no shock stabilization, (ii) first-order viscosity stabilization, (iii) residual-viscosity stabilization.

5. Numerical study II: Burger's equation

In this section we solve Burger's equation in two dimensions. The flux is given by $\mathbf{F}(u) = (\frac{u^2}{2}, \frac{u^2}{2})$, and the velocity field by $\mathbf{F}'(u) = (u, u)$. The exact solution to the considered problem is:

$$u(y, t) = \begin{cases} \begin{cases} -0.2 & \text{if } y_1 < \frac{1}{2} - \frac{3t}{5} \text{ and } \begin{cases} y_2 > \frac{1}{2} + \frac{3t}{20}, \\ \text{otherwise,} \end{cases} \\ 0.5 & \end{cases} \\ \begin{cases} -1 & \text{if } \frac{1}{2} - \frac{3t}{5} < y_1 < \frac{1}{2} - \frac{t}{4} \text{ and } \begin{cases} y_2 > -\frac{8y_1}{7} + \frac{15}{14} - \frac{15t}{28}, \\ \text{otherwise,} \end{cases} \\ 0.5 & \end{cases} \\ \begin{cases} -1 & \text{if } \frac{1}{2} - \frac{t}{4} < y_1 < \frac{1}{2} + \frac{t}{2} \text{ and } \begin{cases} y_2 > \frac{y_1}{6} + \frac{5}{12} - \frac{5t}{24}, \\ \text{otherwise,} \end{cases} \\ 0.5 & \end{cases} \\ \begin{cases} -1 & \text{if } \frac{1}{2} + \frac{t}{2} < y_1 < \frac{1}{2} + \frac{4t}{5} \text{ and } \begin{cases} y_2 > y_1 - \frac{5}{18t} (y_1 + t - \frac{1}{2})^2, \\ \text{otherwise,} \end{cases} \\ \frac{2y_1 - 1}{2t} & \end{cases} \\ \begin{cases} -1 & \text{if } y_1 > \frac{1}{2} + \frac{4t}{5} \text{ and } \begin{cases} y_2 > \frac{1}{2} - \frac{t}{10}, \\ \text{otherwise.} \end{cases} \\ 0.8 & \end{cases} \end{cases} \quad (35)$$

The initial condition simplifies to:

$$u(y, 0) = \begin{cases} -0.2, & \text{if } y_1 < 0.5 \text{ and } y_2 > 0.5, \\ -1, & \text{if } y_1 > 0.5 \text{ and } y_2 > 0.5, \\ 0.5, & \text{if } y_1 < 0.5 \text{ and } y_2 < 0.5, \\ 0.8, & \text{if } y_1 > 0.5 \text{ and } y_2 < 0.5. \end{cases} \quad (36)$$

The initial condition and the exact solution to the considered problem are visualized in Figure 12. A variable time step is chosen as:

$$\Delta t = \text{CFL} \min_{x_i \in X} \left[\frac{h_{\text{loc}}(x_i)}{\sqrt{(F'_1(u(x_i, t)))^2 + (F'_2(u(x_i, t)))^2}} \right], \quad (37)$$

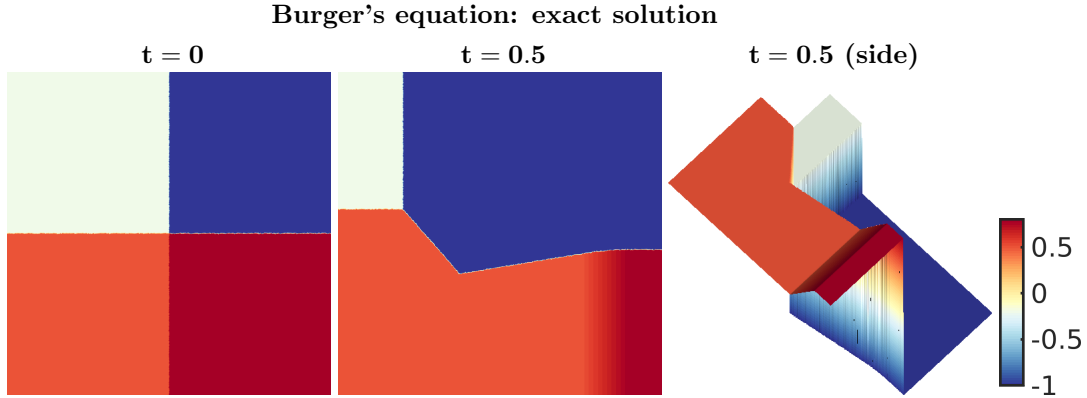


Figure 12: Exact solution to the considered Burger's equation, at time $t = 0$ (initial condition, and at time $t = 0.5$ from two visual perspectives.

where $h_{\text{loc}}(x_i)$ is defined in the scope of (22).

We solve this problem on a unit square $\Omega = [0, 1] \times [0, 1]$ until $t = 0.5$ and use Dirichlet boundary conditions with the data obtained from the exact solution. Our objective is to make observations on how the oversampled RBF-FD method behaves when the nonlinear flux $\mathbf{F}(u)$ is inducing shocks in the solution. We focus on cases when we stabilize the Gibbs phenomenon through P_2 defined in (20) using: (i) first order viscosity (we override (21) by $\varepsilon = \varepsilon_{\text{UV}}$), (ii) residual viscosity (ε as defined in (21)). The hyperviscosity term (13) is always added to the numerical scheme for the purposes of stabilization in time. Throughout this section we use an oversampling parameter $q = 5$ and the CFL number 0.2. The nodes in X point set are generated using the algorithm presented in [29].

First, we examine the numerical solution from a visual perspective in the three cases: when the RBF-FD method is not shock-stabilized, when the method is stabilized with the first-order viscosity and when the method is stabilized using the residual viscosity method. The parameters that we use are $h = 0.005$ ($N = 40000$), $p = 3$ and $q = 5$. The numerical solution is a subject to rapid exponential growth when the Gibbs phenomenon is not stabilized with any of the approaches, and we therefore can not provide any visual results. The solution when the numerical scheme is stabilized using first order viscosity and residual viscosity, is given in Figure 13 and in Figure 14.

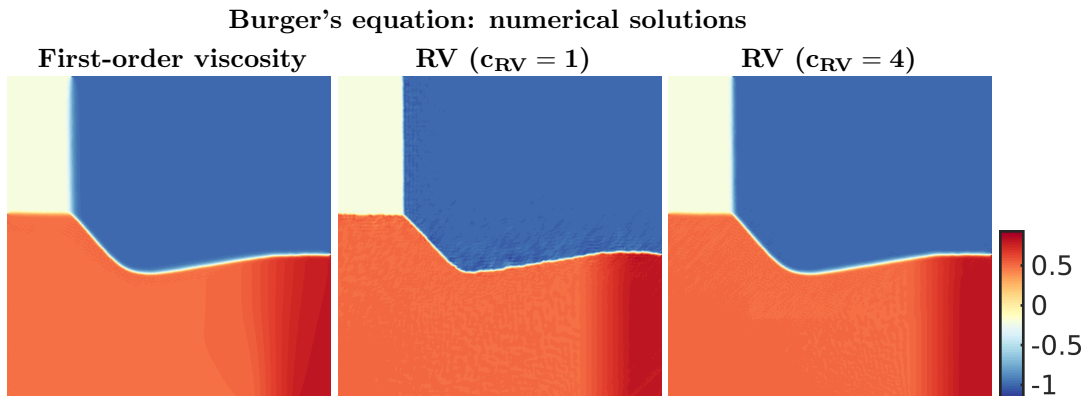


Figure 13: Numerical solutions to the Burger's equations, when the oversampled RBF-FD discretization is shock-stabilized using first-order viscosity, and residual viscosity for two choices of constants C_{RV} in (22). The internodal distance is set to $h = 0.005$ (corresponds to $N = 39504$ unknowns), polynomial degree $p = 3$ is used to construct the stencil-based interpolation problems.

In all cases where we attempted to stabilize the solution, the numerical solution was stable at the end. The smoothest solution is expectedly the one where the first-order viscosity is active throughout Ω . When RV is used, the details around the discontinuities are preserved in a better

way compared with the first-order viscosity solution. The RV solution when c_{RV} in (22) is set to 1 is more oscillatory compared with the RV solution when c_{RV} is set to 4. Despite the oscillations, the important outcome is that the solution is stable in both cases. Here we point out that these solutions are computed on scattered points. We made the same tests on Cartesian points, where we noticed that the oscillations were smaller. In Figure 15 we display the spatial variation of the

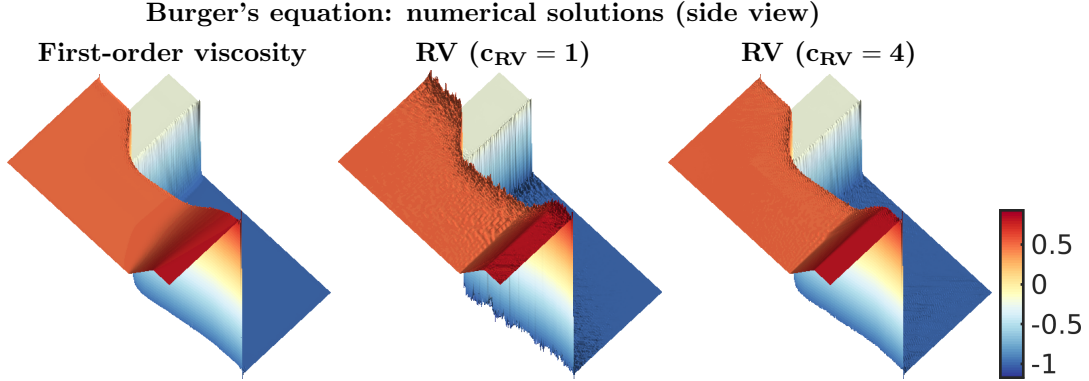


Figure 14: Numerical solutions to the Burger's equations from a rotated perspective, when the oversampled RBF-FD discretization is shock-stabilized using first-order viscosity, and residual viscosity for two choices of constants c_{RV} in (22). The internodal distance is set to $h = 0.005$ (corresponds to $N = 39504$ unknowns), polynomial degree $p = 3$ is used to construct the stencil-based interpolation problems.

viscosity coefficient ε defined in (21), for cases when the first-order viscosity is used and when RV is used. We see that the viscosity coefficient is large only in the vicinity of the shock, when RV is used, thus, the shocks are well captured.

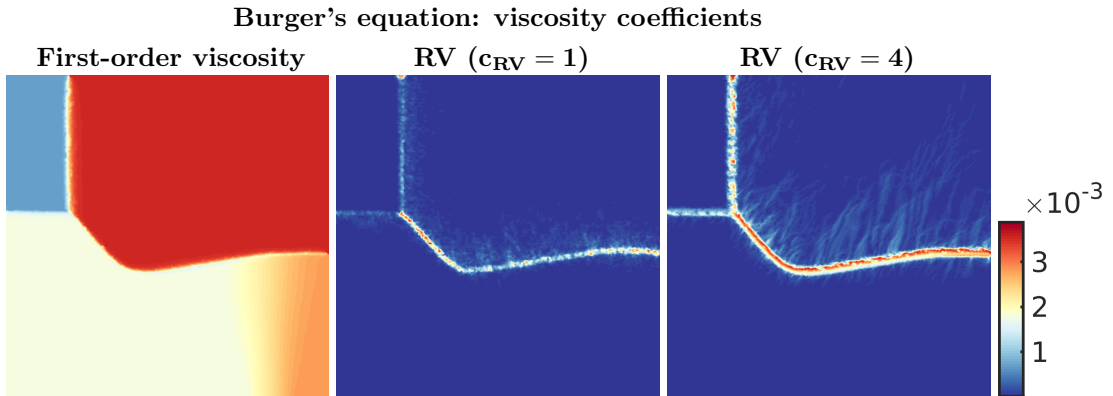


Figure 15: Spatial variation of the viscosity coefficients, when the oversampled RBF-FD discretization is shock-stabilized using first-order viscosity, and residual viscosity for two choices of constants c_{RV} in (22). The internodal distance is set to $h = 0.005$ (corresponds to $N = 39504$ unknowns), polynomial degree $p = 3$ is used to construct the stencil-based interpolation problems.

In Figure 16 and Figure 17, we display the convergence under node refinement, in 2-norm and 1-norm respectively, where the norms are defined in (33). The optimal convergence rates are expected to be 0.5 and 1. The convergence trends in all stabilized cases are close to these optimal rates. When stabilizing the scheme using the first-order viscosity, the error is constant-wise larger compared to when stabilizing the scheme using RV. We do not observe that an increase of p would – in the present case – lead to a significant improvement of the error by means of a constant.

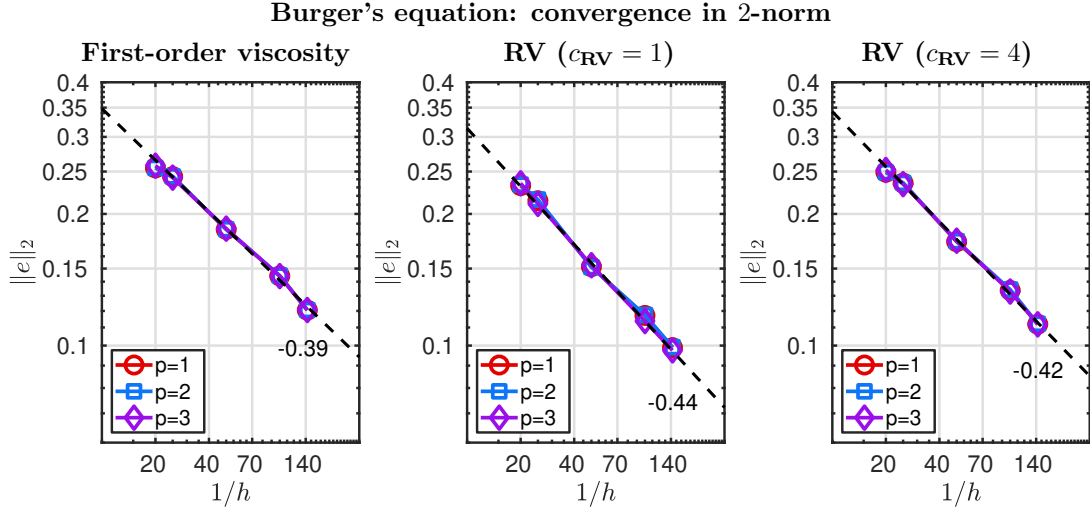


Figure 16: Convergence in 2-norm, under node refinement for different choices of the monomial basis degree p , used to construct the stencil-based approximants. The convergence plots are displayed for cases when the oversampled RBF-FD is shock-stabilized using first-order viscosity and the residual viscosity.

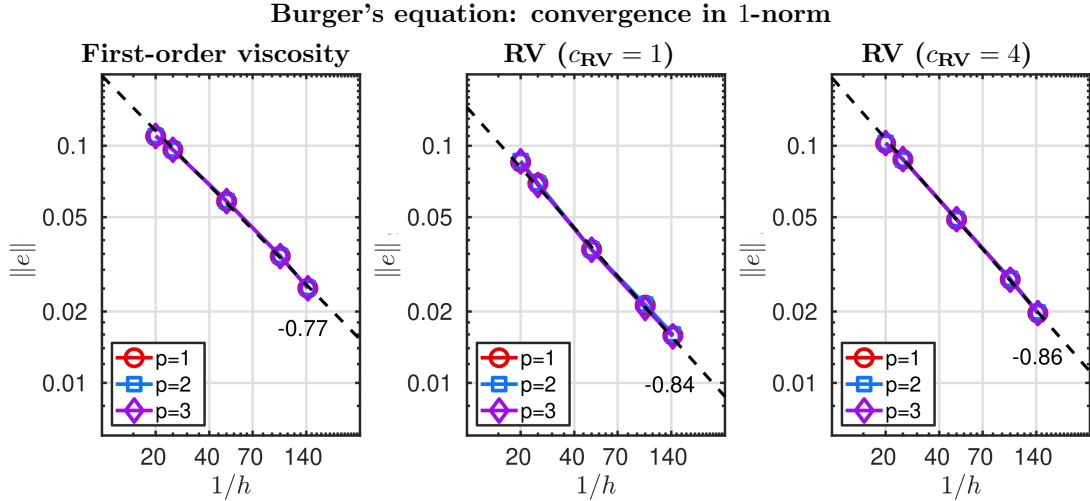


Figure 17: Convergence in 1-norm, under node refinement for different choices of the monomial basis degree p , used to construct the stencil-based approximants. The convergence plots are displayed for cases when the oversampled RBF-FD is shock-stabilized using first-order viscosity and the residual viscosity.

6. Numerical study III: The Kurganov-Petrova-Popov rotating wave problem

We solve another scalar conservation law with a nonlinear flux: the Kurganov-Petrova-Popov (KPP) problem, initially introduced in [41]. The flux is given by $\mathbf{F}(u) = (\sin u, \cos u)$. The computational domain is a square $\Omega = [-2, 1.5] \times [2, 2.5]$. The initial condition and the Dirichlet boundary condition are in the same order defined as:

$$u(y, 0) = \begin{cases} \frac{14\pi}{4} & \text{if } \sqrt{y_1^2 + y_2^2} \leq 1, \\ \frac{\pi}{4} & \text{otherwise.} \end{cases}, \quad u(y, t)|_{\partial\Omega} = \frac{\pi}{4}. \quad (38)$$

We use the monomial basis degree $p = 3$ to construct the stencil based approximations, on a scattered point set X with a mean internodal distance $h = 0.02$ (corresponding to 39498 nodes). The point set is obtained using the algorithm introduced in [29]. The oversampling parameter is set to $q = 5$

and the RV constant to $C_{RV} = 3$. We run the simulation until time $t = 1$ with the CFL number 0.2. Since the velocity field is for this benchmark rotational we use a fixed time step Δt , computed according to (32).

The solution at $t = 1$ when the shocks are not stabilized is displayed in Figure 18, where we see oscillations so large, that the solution can not be seen as physical. Stabilized solutions are displayed

The KPP problem: unstabilized numerical solutions

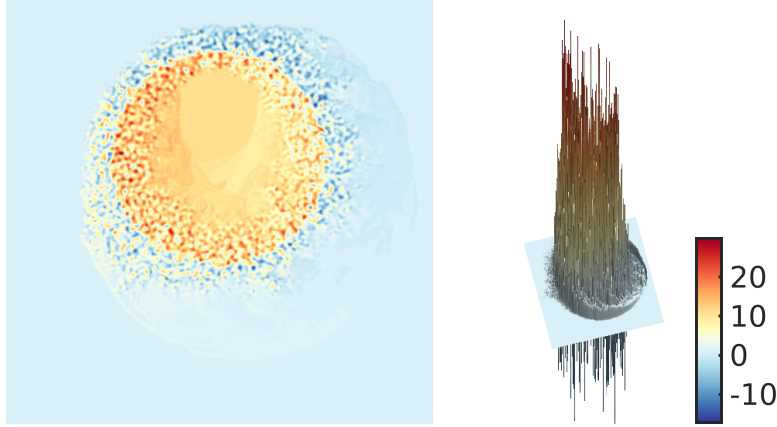


Figure 18: Solution to the Kurganov-Petrova-Popov problem, when no shock stabilization is added to the oversampled RBF-FD discretization. The hyperviscosity term in (12) is active in order to stabilize the numerical scheme in time.

in Figure 19. The solutions stabilized with the first-order viscosity and the residual viscosity are in an overall sense similar. A closer look, however, reveals that the residual viscosity solution includes sharper details along the edge of the spiral. The RV solution is less diffused compared to the first-order viscosity solution. The viscosity coefficients are given in Figure 20, where we see that the residual viscosity is, roughly speaking, only active in the region of the discontinuity.

7. Numerical study IV: compressible Euler equations

In this section we solve compressible Euler equations discretized in (18). The Euler system can be seen as a limiting case of the Navier-Stokes system of equations, when the physical viscosity term tends to 0. We solve several benchmarks which model a fluid in the state of a compressed gas. For all experiments we use the adiabatic constant $C_{ad} = 1.4$. The variable time steps for all considered cases are computed according to the formula:

$$\Delta t = \text{CFL} \min_{x_i \in X} \left[\frac{h_{\text{loc}}(x_i)}{\sqrt{v_1^2(x_i, t) + v_2^2(x_i, t) + C_{ad} p(x_i, t) / \rho(x_i, t)}} \right], \quad (39)$$

where h_{loc} is defined within the context of (22). The approximation errors for each unknown function are computed analogously to (33).

7.1. Sod's shock tube problem

The computational domain is a rectangle $\Omega = [0, 1] \times [0, 0.4]$, in which two fluids with different physical properties are separated by a membrane positioned at $y_1 = 0.5$. The initial condition is given by:

$$\begin{aligned} y_1 < 0.5 : \quad & \rho = 1, \quad \mathbf{v} = (0, 0), \quad p = 1, \\ y_1 > 0.5 : \quad & \rho = 0.125, \quad \mathbf{v} = (0, 0), \quad p = 0.1. \end{aligned} \quad (40)$$

The simulation of the two fluids is started by removing the membrane at $t = 0$, the final state is observed at $t = 0.25$. The boundary condition is *slip* ($\mathbf{v} \cdot \mathbf{n} = 0$) along all boundaries of the rectangle, where \mathbf{n} is the outward pointing normal.

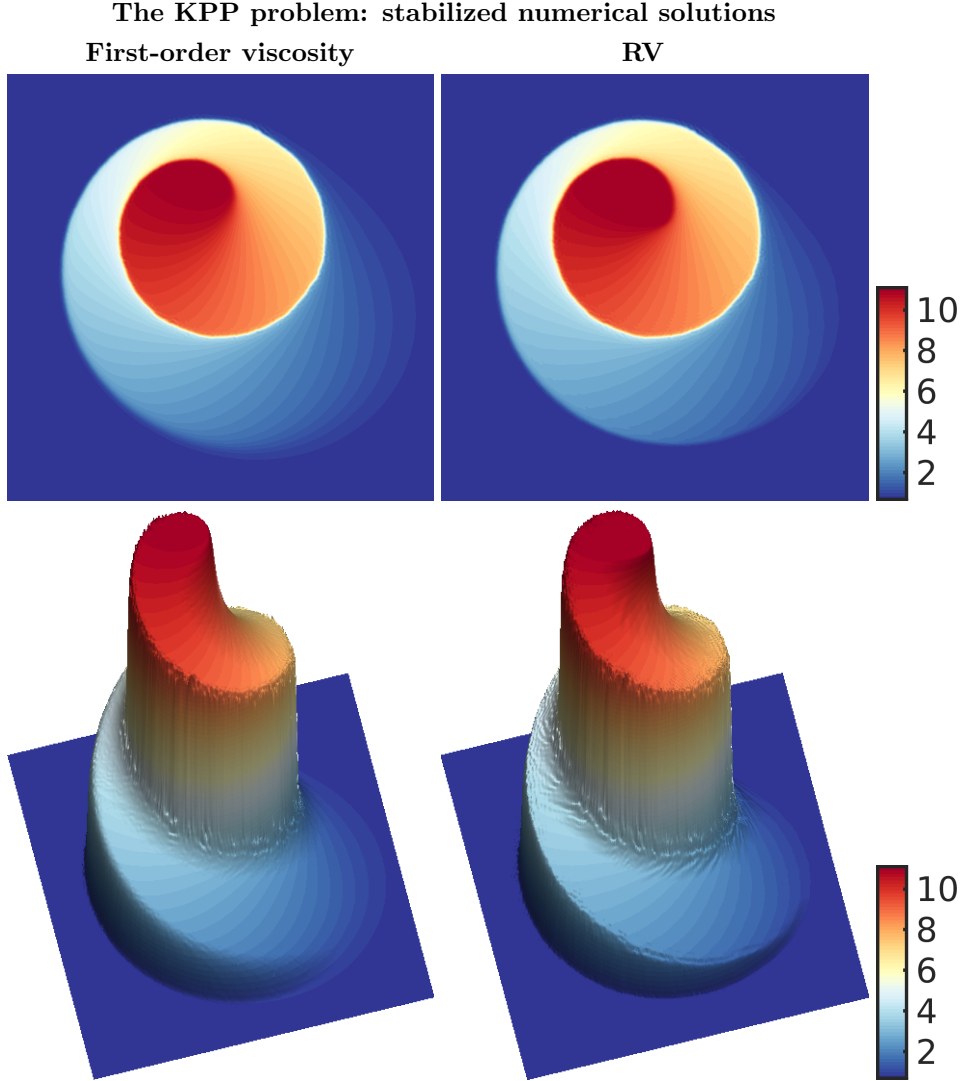


Figure 19: A numerical solution to the Kurganov-Petrova-Popov problem from a top perspective (first row) and a side perspective (second row), when two different shock stabilizations are added to the oversampled RBF-FD discretization. The hyperviscosity term in (12) is active in addition, in order to stabilize the numerical scheme in time.

We use scattered nodes generated using an algorithm from [29] to discretize Ω . Throughout the section, the CFL condition is set to 0.2, the oversampling parameter is set to $q = 5$ and the monomial basis degree to $p = 3$, if not stated otherwise.

The numerical solution (density), obtained using the RV stabilized oversampled RBF-FD method, is displayed in Figure 21. We observe that the shock discontinuity and the contact discontinuity are well captured. The mean distance between the computational nodes is set to $h = 0.003$ ($N = 22244$ unknowns).

Now we compare the RV stabilized RBF-FD solution with the exact solution. The exact solution is obtained for an equivalent problem in one dimension. We interpolate the 2-dimensional RBF-FD solution along the line $y_2 = 0.2$ in order to obtain an approximate 1-dimensional solution. This can be done since the variation of the 2-dimensional solution in the y_2 direction is very small. The first result is displayed in Figure 22, where we show exact and numerical profiles of the density and the temperature. We observe that the discontinuous exact solution is well approximated by the numerical solution, and that the approximation gets increasingly better with a decreasing h . In Figure 23 we plot the 2-norm convergence of the numerical solution along the line $y_2 = 0.2$, where

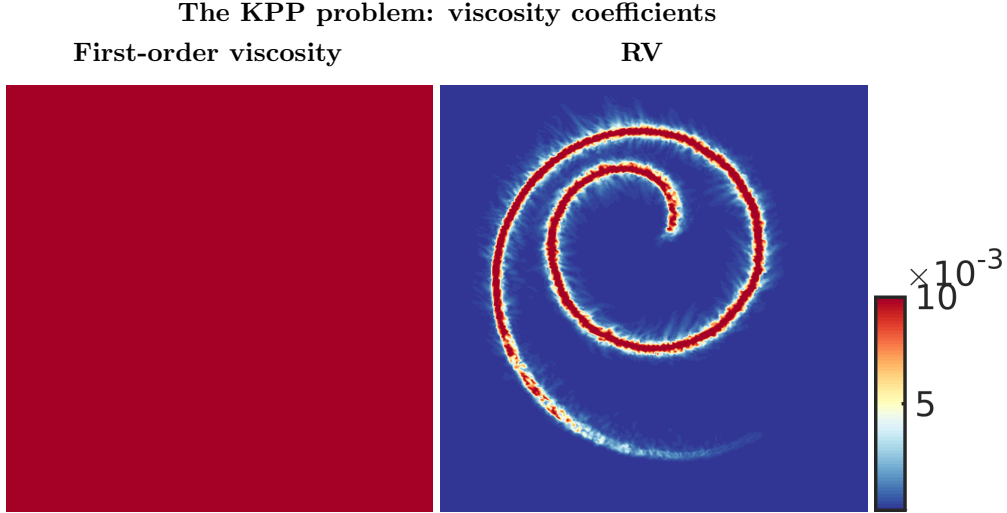


Figure 20: The images display the spatial variation of the viscosity coefficient when using the first-order viscosity and the residual viscosity.

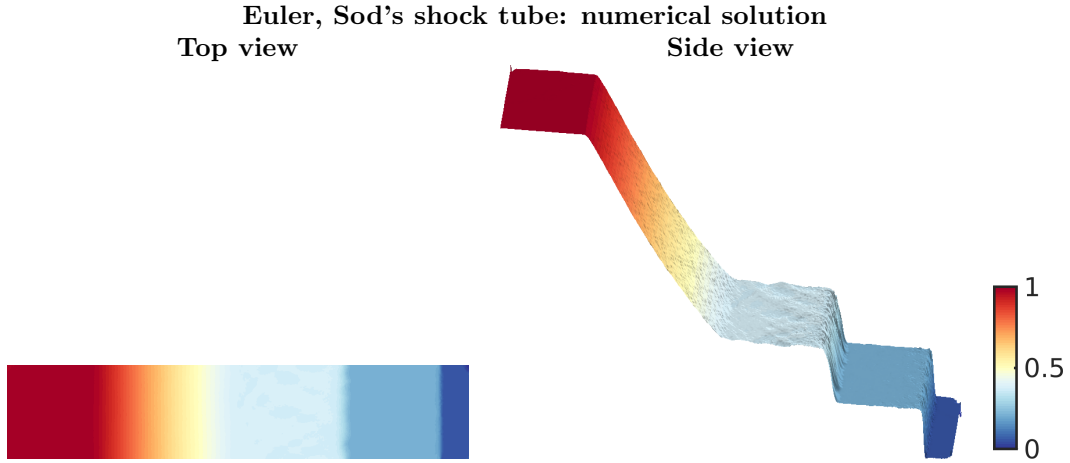


Figure 21: The numerical solution (density ρ) of Sod's shock tube problem at $t = 0.25$, computed using the oversampled RBF-FD method. The internodal distance is set to $h = 0.003$ (corresponds to $N = 22244$ unknowns). The monomial basis degree used to construct the stencil-based approximants is $p = 3$. The oversampling parameter is set to $q = 5$.

the exact 1D solution is taken as a reference. The optimal convergence rates for this norm are expected to be 0.5. For the density and the momentum, our convergence rates are optimal, while the convergence rate for the total energy is slightly higher than optimal. We also observe that for the density, the approximation error in $p = 3$ case is slightly smaller compared to $p = 2$ and $p = 1$. In Figure 24 we show an analogous convergence plot, but in 1-norm. Here the optimal convergence rate is 1. The convergence plots in all cases are close to the optimum. An increase in p gives a slight improvement of the approximation error by means of a constant.

In [40], the authors used the RV stabilized finite element method to solve Sod's shock tube problem using the same set of physical parameters. Comparing Figure 23 and Figure 24 from the present paper, with Figure 6 from [40], we can observe that the errors in 2-norm and 1-norm are comparable in magnitude and the slopes.

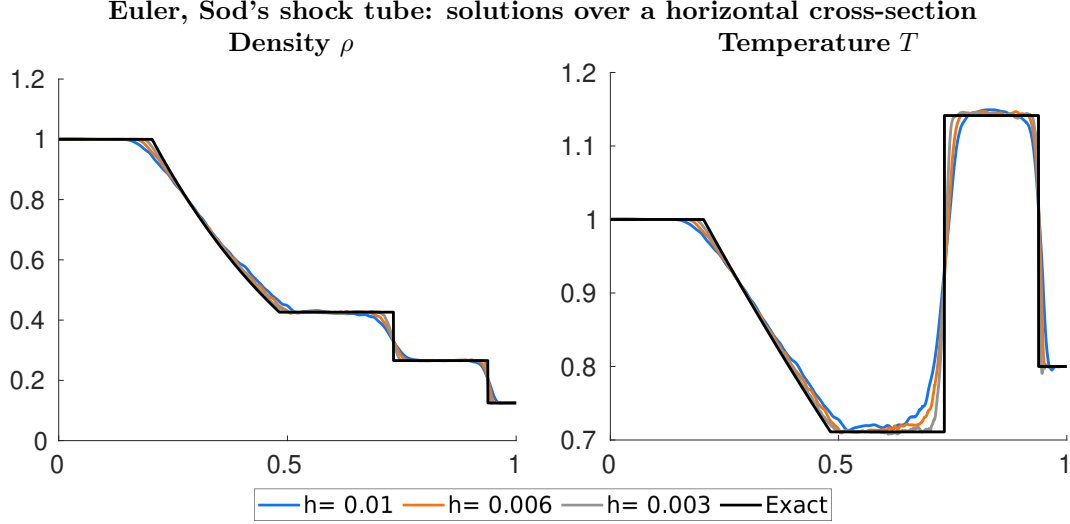


Figure 22: A slice of the solution of Sod's shock tube problem at $t = 0.25$, computed using the oversampled RBF-FD method. The numerical solutions for different h are compared with the exact solution. The monomial basis degree used to construct the stencil-based approximants is $p = 3$. The oversampling parameter is set to $q = 5$.

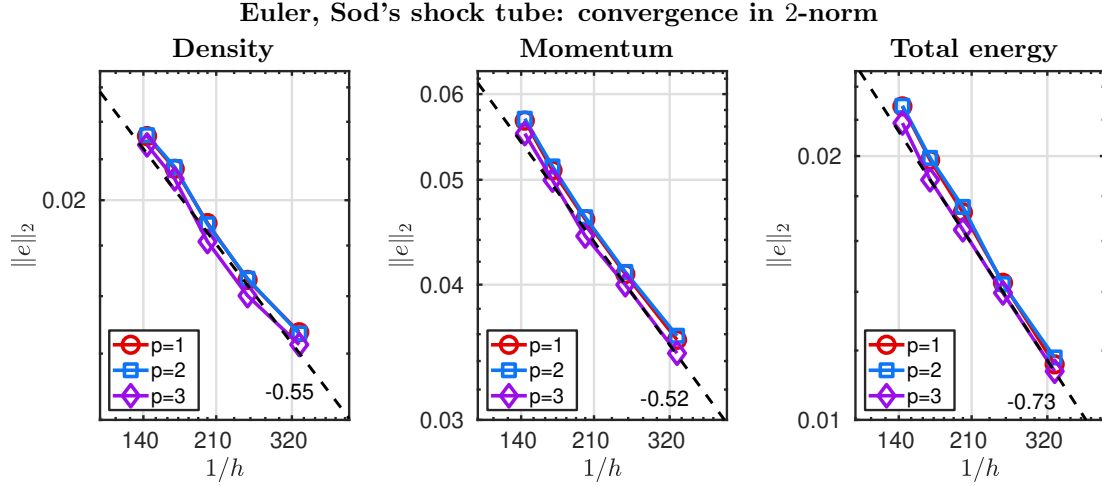


Figure 23: Convergence in 2-norm under node refinement, for different choices of the monomial basis degree p , used to construct the stencil-based approximants.

7.2. A 2D Riemann problem

The domain is a square $\Omega = [0, 1] \times [0, 1]$. The initial condition is defined such that it takes different values in different quadrants of the square:

$$\begin{aligned}
 \rho = 4/5, \quad p = 1, \quad \mathbf{v} = (0, 0), & \quad \text{in } 0 < y_1 < 0.5, \quad 0 < y_2 < 0.5, \\
 \rho = 1, \quad p = 1, \quad \mathbf{v} = (0.7276, 0), & \quad \text{in } 0 < y_1 < 0.5, \quad 0.5 < y_2 < 1, \\
 \rho = 1, \quad p = 1, \quad \mathbf{v} = (0, 0.7276), & \quad \text{in } 0.5 < y_1 < 1, \quad 0 < y_2 < 0.5, \\
 \rho = 17/32, \quad p = 2/5, \quad \mathbf{v} = (0, 0), & \quad \text{in } 0.5 < y_1 < 1, \quad 0.5 < y_2 < 1.
 \end{aligned} \tag{41}$$

The boundary conditions are *slip* on the top side and the right side of the square domain. On the bottom and the left side of the square domain, we use the inflow Dirichlet boundary conditions. These are for all t set to the corresponding values of the initial condition. The scattered nodes over Ω are placed using the algorithm provided in [29]. We set the monomial basis degree to $p = 3$, the

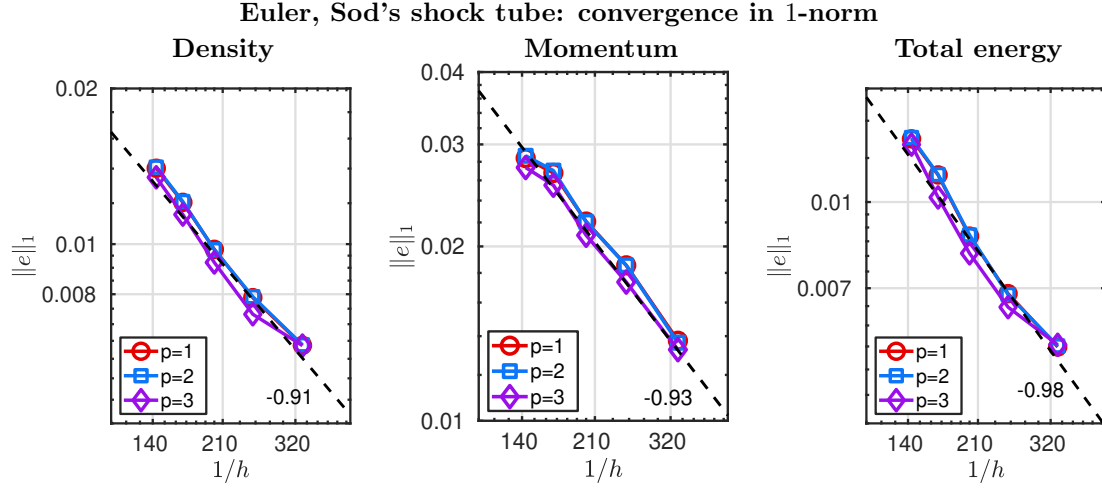


Figure 24: Convergence in 1-norm under node refinement, for different choices of the monomial basis degree p , used to construct the stencil-based approximants.

oversampling parameter to $q = 5$, the internodal distance to $h = 0.0025$ (corresponds to $N = 156981$ unknowns), the CFL number to 0.2 and the RV constant to $C_{RV} = 3$, and run the simulation until $t = 0.25$.

The result is given in Figure 25, where we display the RBF-FD solution stabilized using RV and the corresponding spatial distribution of the viscosity coefficient. We observe that the solution is sharp around the shock in the upper right corner of the domain, and that the contact discontinuity in the lower left quadrant is well defined. Furthermore, the magnitude of the viscosity coefficient is largest in the shock region and slightly smaller in the region of the contact discontinuity. The solution looks very similar to the one obtained using the RV stabilized finite element method in Figure 7 of [40], and also to all of the solutions obtained using six different shock-capturing schemes in Figure 4.2 of [42].

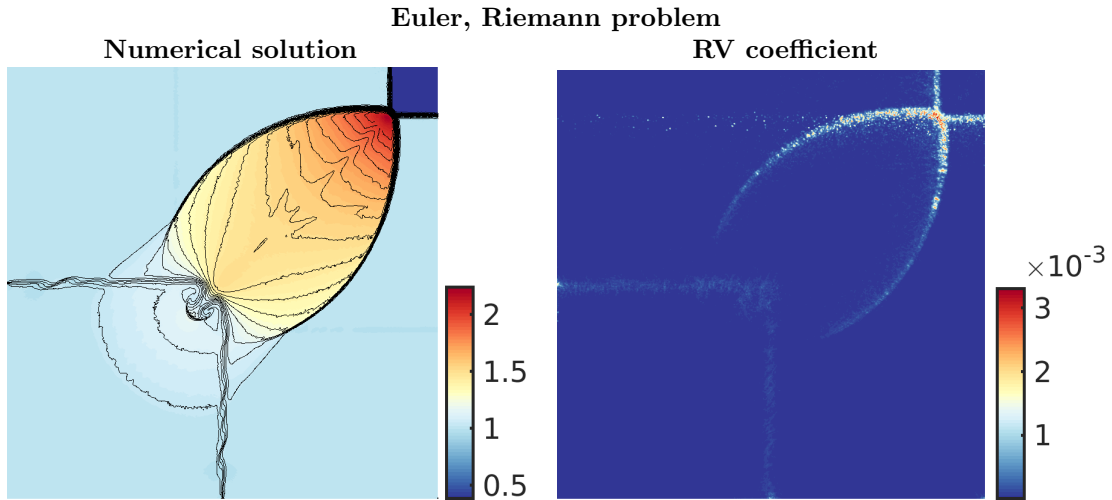


Figure 25: The numerical solution of the Riemann problem, together with the spatial distribution of the residual viscosity coefficient. The colormap of the numerical solution shows the pressure in the interval $[0.37, 2.23]$, while the contour lines show the density in the interval $[0.54, 1.7]$.

7.3. A channel flow over a forward facing step

We study a Mach 3 supersonic flow over a forward facing step in a rectangular channel $\Omega = [0, 3] \times [0, 1]$. The sharp inward corner of the forward facing step is located at coordinate $(0.6, 0.2)$. The initial condition is: $\rho = 1.4$, $\mathbf{m} = (4.2, 0)$, $\mathcal{E} = 8.8$. We use slip boundary conditions on the top and the bottom boundaries of the channel. On the left boundary of the channel we use an inflow (Dirichlet) boundary condition, where for all t we prescribe the values of the initial condition. On the right side of the channel we mimic the outflow by not imposing any boundary conditions. We run the simulation until $t = 4$ using $N = 117432$ nodes obtained using Gmsh [30]. Other parameters are $C_{RV} = 5$, $CFL = 0.3$. We also consider two choices of monomial basis degrees: $p = 1$ and $p = 3$.

The flow entering the channel hits the step and then creates a bow shock that propagates towards the upper boundary, and then keeps reflecting between upper and lower boundaries. Close to the first reflection where the shocks meet, there is a so-called triple point. From the direction of the triple point towards the outflow, the physical solution has a contact discontinuity, which is challenging to capture in a numerical sense.

The numerical results are collected in Figure 26. The numerical solutions for $p = 1$ and $p = 3$ are similar to the solutions displayed in Figure 9 of [40]. A prevailing difference is that the shock reflection close to the inward facing corner has a different location. This is ascribed to the fact that in this paper we do not smooth out the inward corner as the authors in [40] do, but keep it sharp. In our case, the contact discontinuity is captured for both choices of p . When $p = 1$ we notice that the solution around the reflection closest to the outflow of the channel, has a large error by means of the phase, compared to when using $p = 3$. This shows a benefit of using a high-order discretization, even if the underlying solution does not have a sufficient regularity to support the high-order convergence.

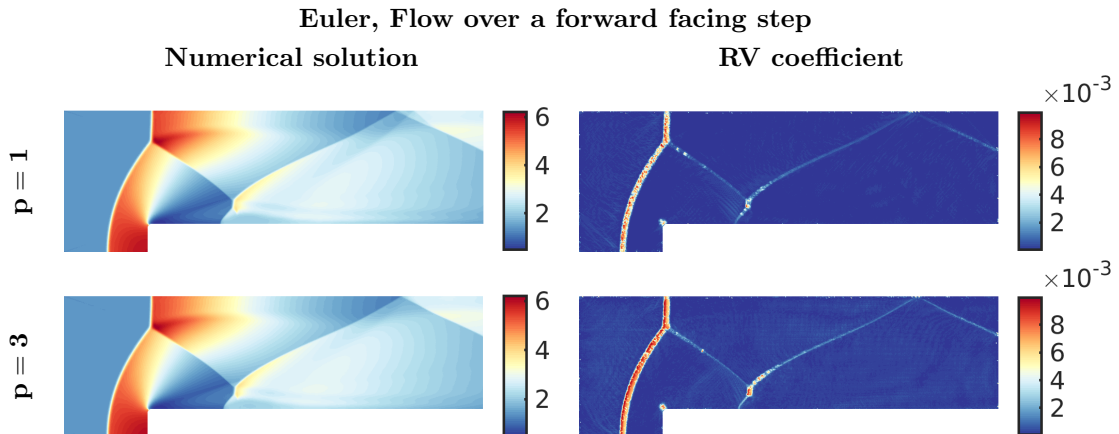


Figure 26: The results are made using $N = 117432$ nodes. The numerical solution (left column) is given in terms of density ρ at $t = 4$, for two choices of a monomial basis degree p to construct the stencil based approximation. The plots in the right column are residual viscosity coefficients for the two choices of p .

7.4. Explosion in a domain with cylinders

This problem was initially introduced in [40]. The computational domain is the disc with radius 2. In addition, the domain has eight inner circular boundaries with radius 0.3, which are placed at distance 1.4 from the origin. The distance between the neighboring inner circular boundaries are equal. The initial condition is a discontinuous function, where a compressed gas with $\rho = 1$, $p = 1$ is put inside the disc with radius $\sqrt{0.4}$, located at the origin. Outside of that disc we have $\rho = 0.125$ and $p = 1$. The velocity is $\mathbf{v} = (0, 0)$ throughout the domain. Slip boundary conditions are used for the exterior boundary and all of the interior boundaries. The simulation is run until $t = 4.25$.

We use $N = 337356$ nodes obtained using Gmsh [30]. Other parameters are: $p = 3$, $C_{RV} = 3$ and $CFL = 0.3$. The results are given in Figure 27, where we observe that RV performs well, even

in cases where the numerical solution exhibits small details. The spatial distribution of the residual viscosity coefficient is displayed in Figure 28, where we see that the action of viscosity is localized.

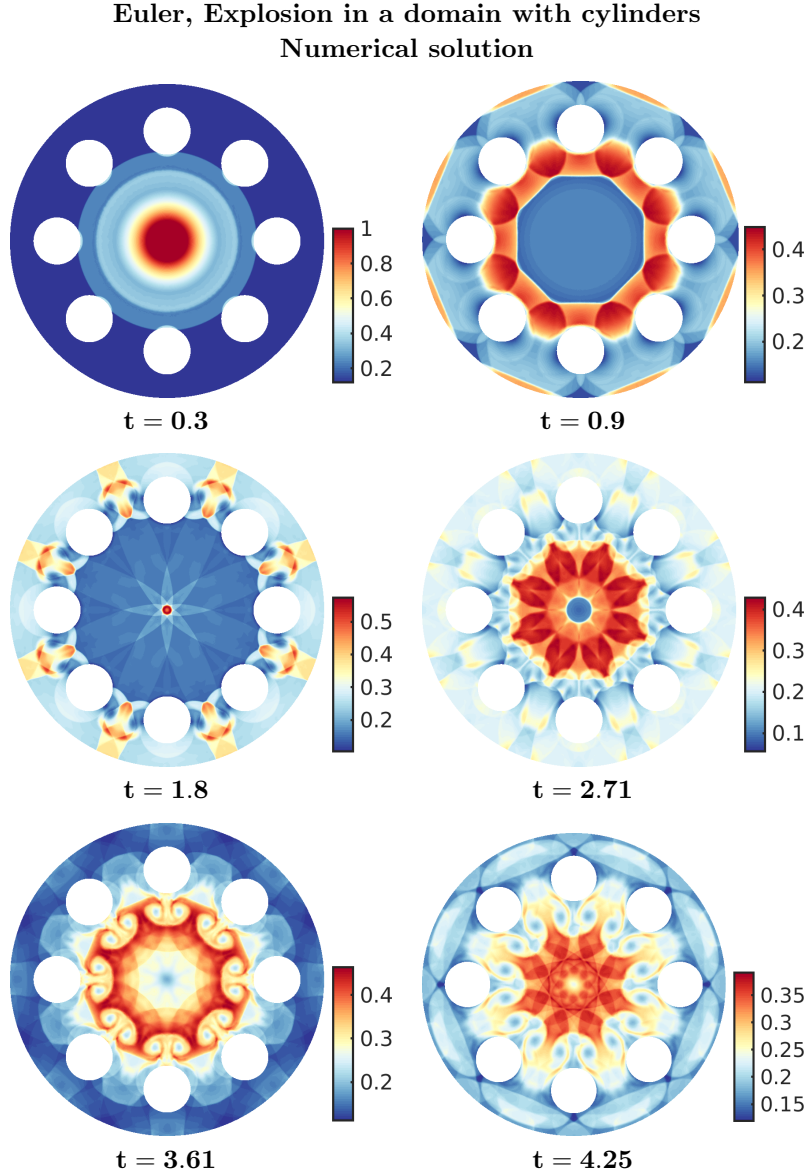


Figure 27: Numerical solution of the benchmark Explosion in a domain with cylinders, at different points in time t . The solution is obtained using $N = 337356$ nodes. The oversampling parameter is $q = 5$. The polynomial degree used to construct the stencil-based approximation is $p = 3$.

8. Final discussion

In this paper we covered several aspects of discretizing conservation laws using the RBF-FD method.

We observed that oversampling by itself does not improve the time stability of the RBF-FD method. A theoretical argumentation for this behavior and further analysis is going to be given in a future paper [43].

Another observation is that the collocation RBF-FD method is nearly as accurate as the over-sampled RBF-FD method when using Dirichlet boundary conditions. Although not examined in

Euler, Explosion in a domain with cylinders
Residual viscosity coefficient

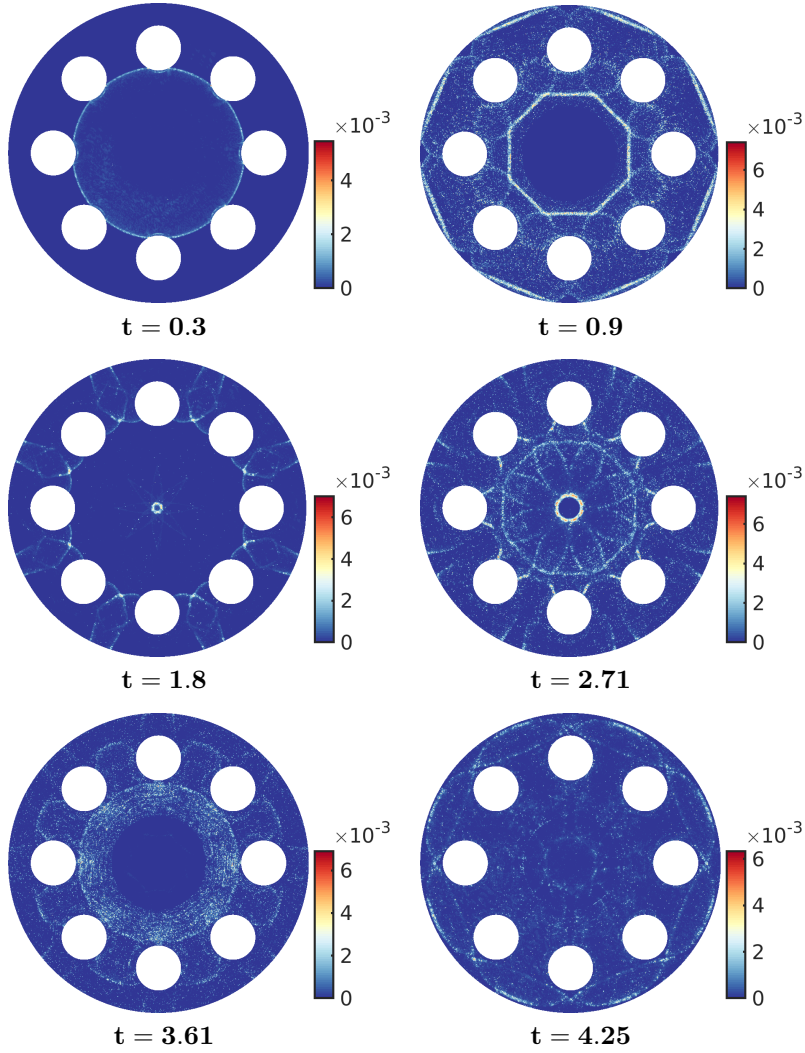


Figure 28: Spatial distribution of the residual viscosity coefficient used to compute the solution of the benchmark Explosion in a domain with cylinders. The coefficient is displayed at different points in time t . The corresponding solution is computed obtained using $N = 337356$ nodes. The oversampling parameter is $q = 5$. The polynomial degree used to construct the stencil-based approximation is $p = 3$.

this paper, we believe that if we had used Neumann boundary conditions, the collocation RBF-FD discretization would have suffered from the same type of instability as observed and studied in [8], leading to worse approximation errors compared with the errors of the oversampled RBF-FD method.

The RV constant C_{RV} which is defined by the user is not a sensitive parameter. We did, however, notice that C_{RV} had to be chosen larger than 1, when the magnitude of the numerical solution was large. This was not observed when RV was combined with the finite element methods, for example in [40]. We did not fully explore the reasons behind that. A speculative explanation is that we used a different residual definition compared to the residual definition used in [40].

We found that a symmetric hyperviscosity operator (13) is an effective stabilization in time. The residual as defined in the present work turned out to be an excellent indicator of discontinuities. The residual viscosity stabilization (RV) is consistent when the solution is smooth.

Finally, all experiments confirmed that a combination of the RBF-FD method and the RV stabilization provides a robust framework for discretizing nonlinear conservation laws in scalar and system settings.

Acknowledgments

We thank (in alphabetical order) Lukas Lundgren, Tuan Anh Dao and Vidar Stiernström from Uppsala University for fruitful discussions about time-dependent conservation laws.

Appendix A. A high-order time derivative approximation

```
function w = timedderivatives (t)
    % Input: a vector t, where t(i) is time at which the solution is available.
    % Output: a vector w, where each w(i) is used to multiply u|_{t(i)} in order
    % ... to get a derivative at t(end).
    % Usage: d/dt u(t_end) = w(end)*u(end) + w(end-1)*u(end-1) + ... + w(1)*u(1),
    % ... where t_end is the time at which the last solution point is available.

    scale = 1/max(abs(t));
    t = t*scale;
    t_eval = t(end); % The derivative should be evaluated at t(end).

    % Construct the polynomial basis, and differentiate it in a point t_eval.
    A = zeros(size(t,1), size(t,1));
    b_t = zeros(1, size(t,1));
    for k=1:length(t)
        A(:,k) = t.^(k-1);
        b_t(k) = (k-1)*t_eval.^(k-2);
    end
    w = scale*(b_t*inv(A));

end
```

References

References

- [1] J. M. Martel, R. B. Platte, [Stability of radial basis function methods for convection problems on the circle and sphere](#), *J. Sci. Comput.* 69 (2) (2016) 487–505. doi:10.1007/s10915-016-0206-9. URL <https://doi.org/10.1007/s10915-016-0206-9>
- [2] A. I. Tolstykh, On using RBF-based differencing formulas for unstructured and mixed structured-unstructured grid calculations, in: *Proceedings of the 16th IMACS World Congress on Scientific Computation, Applied Mathematics and Simulation, Lausanne, Switzerland, 2002*.
- [3] N. Flyer, G. A. Barnett, L. J. Wicker, Enhancing finite differences with radial basis functions: experiments on the Navier-Stokes equations, *J. Comput. Phys.* 316 (2016) 39–62. doi:10.1016/j.jcp.2016.02.078.
- [4] E. Lehto, V. Shankar, G. B. Wright, [A radial basis function \(RBF\) compact finite difference \(FD\) scheme for reaction-diffusion equations on surfaces](#), *SIAM J. Sci. Comput.* 39 (5) (2017) A2129–A2151. doi:10.1137/16M1095457. URL <https://doi.org/10.1137/16M1095457>

- [5] N. Talat, B. Mavrič, V. Hatić, S. Bajt, B. Šarler, [Phase field simulation of Rayleigh-Taylor instability with a meshless method](#), *Eng. Anal. Bound. Elem.* 87 (2018) 78–89. doi:10.1016/j.enganabound.2017.11.015.
URL <https://doi.org/10.1016/j.enganabound.2017.11.015>
- [6] J. M. Berljavac, P. K. Mishra, J. Slak, G. Kosec, [Rbf-fd analysis of 2d time-domain acoustic wave propagation in heterogeneous media](#), *Computers and Geosciences* 153 (2021) 104796. doi:https://doi.org/10.1016/j.cageo.2021.104796.
URL <https://www.sciencedirect.com/science/article/pii/S0098300421000984>
- [7] V. Shankar, [The overlapped radial basis function-finite difference \(RBF-FD\) method: a generalization of RBF-FD](#), *J. Comput. Phys.* 342 (2017) 211–228. doi:10.1016/j.jcp.2017.04.037.
URL <https://doi.org/10.1016/j.jcp.2017.04.037>
- [8] I. Tominec, E. Larsson, A. Heryudono, [A least squares radial basis function finite difference method with improved stability properties](#), *SIAM J. Sci. Comput.* 43 (2) (2021) A1441–A1471. doi:10.1137/20M1320079.
URL <https://doi.org/10.1137/20M1320079>
- [9] V. Shankar, G. B. Wright, A. Narayan, [A robust hyperviscosity formulation for stable RBF-FD discretizations of advection-diffusion-reaction equations on manifolds](#), *SIAM J. Sci. Comput.* 42 (4) (2020) A2371–A2401. doi:10.1137/19M1288747.
URL <https://doi.org/10.1137/19M1288747>
- [10] V. Shankar, G. B. Wright, A. L. Fogelson, [An efficient high-order meshless method for advection-diffusion equations on time-varying irregular domains](#), *Journal of Computational Physics* (2021) 110633doi:https://doi.org/10.1016/j.jcp.2021.110633.
URL <https://www.sciencedirect.com/science/article/pii/S0021999121005283>
- [11] B. Fornberg, E. Lehto, [Stabilization of RBF-generated finite difference methods for convective PDEs](#), *J. Comput. Phys.* 230 (6) (2011) 2270–2285. doi:10.1016/j.jcp.2010.12.014.
URL <https://doi.org/10.1016/j.jcp.2010.12.014>
- [12] N. Flyer, E. Lehto, S. Blaise, G. B. Wright, A. St-Cyr, [A guide to RBF-generated finite differences for nonlinear transport: shallow water simulations on a sphere](#), *J. Comput. Phys.* 231 (11) (2012) 4078–4095. doi:10.1016/j.jcp.2012.01.028.
URL <https://doi.org/10.1016/j.jcp.2012.01.028>
- [13] J. Von Neumann, R. D. Richtmyer, [A method for the numerical calculation of hydrodynamic shocks](#), *J. Appl. Phys.* 21 (1950) 232–237.
- [14] C. Johnson, A. Szepessy, P. Hansbo, [On the convergence of shock-capturing streamline diffusion finite element methods for hyperbolic conservation laws](#), *Math. Comp.* 54 (189) (1990) 107–129. doi:10.2307/2008684.
URL <https://doi.org/10.2307/2008684>
- [15] M. Nazarov, [Convergence of a residual based artificial viscosity finite element method](#), *Comput. Math. Appl.* 65 (4) (2013) 616–626. doi:10.1016/j.camwa.2012.11.003.
URL <https://doi.org/10.1016/j.camwa.2012.11.003>
- [16] J.-L. Guermond, R. Pasquetti, B. Popov, [Entropy viscosity method for nonlinear conservation laws](#), *J. Comput. Phys.* 230 (11) (2011) 4248–4267. doi:10.1016/j.jcp.2010.11.043.
URL <https://doi.org/10.1016/j.jcp.2010.11.043>
- [17] M. Nazarov, J. Hoffman, [Residual-based artificial viscosity for simulation of turbulent compressible flow using adaptive finite element methods](#), *Internat. J. Numer. Methods Fluids* 71 (3) (2013) 339–357. doi:10.1002/flid.3663.
URL <https://doi.org/10.1002/flid.3663>

- [18] V. Stiernström, L. Lundgren, M. Nazarov, K. Mattsson, [A residual-based artificial viscosity finite difference method for scalar conservation laws](#), *J. Comput. Phys.* 430 (2021) 110100. doi:10.1016/j.jcp.2020.110100. URL <https://doi.org/10.1016/j.jcp.2020.110100>
- [19] S. Marras, M. Nazarov, F. X. Giraldo, [Stabilized high-order Galerkin methods based on a parameter-free dynamic SGS model for LES](#), *J. Comput. Phys.* 301 (2015) 77–101. doi:10.1016/j.jcp.2015.07.034. URL <https://doi.org/10.1016/j.jcp.2015.07.034>
- [20] L. Lu, M. Nazarov, P. Fischer, [Nonlinear artificial viscosity for spectral element methods](#), *C. R. Math. Acad. Sci. Paris* 357 (7) (2019) 646–654. doi:10.1016/j.crma.2019.07.006. URL <https://doi.org/10.1016/j.crma.2019.07.006>
- [21] B. Engquist, A. Harten, S. Osher, [A high order essentially nonoscillatory shock capturing method](#), in: *Large scale scientific computing* (Oberwolfach, 1985), Vol. 7 of *Progr. Sci. Comput.*, Birkhäuser Boston, Boston, MA, 1987, pp. 197–208. doi:10.1007/BF01061328. URL <https://doi.org/10.1007/BF01061328>
- [22] X.-D. Liu, S. Osher, T. Chan, [Weighted essentially non-oscillatory schemes](#), *J. Comput. Phys.* 115 (1) (1994) 200–212. doi:10.1006/jcph.1994.1187. URL <https://doi.org/10.1006/jcph.1994.1187>
- [23] F. Mönkeberg, [High-order essentially nonoscillatory methods based on radial basis functions](#) (2020) 196doi:10.5075/epfl-thesis-8411. URL <http://infoscience.epfl.ch/record/279487>
- [24] J. S. Hesthaven, F. Mönkeberg, [Two-dimensional RBF-ENO method on unstructured grids](#), *J. Sci. Comput.* 82 (3) (2020) Paper No. 76, 24. doi:10.1007/s10915-020-01176-2. URL <https://doi.org/10.1007/s10915-020-01176-2>
- [25] J. S. Hesthaven, F. Mönkeberg, [Hybrid high-resolution RBF-ENO method](#), *J. Comput. Phys.* X 12 (2021) 100089. doi:10.1016/j.jcpx.2021.100089. URL <https://doi.org/10.1016/j.jcpx.2021.100089>
- [26] P. L. Roe, [Characteristic-based schemes for the Euler equations](#), in: *Annual review of fluid mechanics*, Vol. 18, Annual Reviews, Palo Alto, CA, 1986, pp. 337–365.
- [27] B. van Leer, [Towards the ultimate conservative difference scheme. V. A second-order sequel to Godunov’s method](#) [*J. Comput. Phys.* **32** (1979), no. 1, 101–136], Vol. 135, 1997, pp. 227–248, with an introduction by Ch. Hirsch, Commemoration of the 30th anniversary {of *J. Comput. Phys.*}. doi:10.1006/jcph.1997.5757. URL <https://doi.org/10.1006/jcph.1997.5757>
- [28] A. Kurganov, E. Tadmor, [Solution of two-dimensional Riemann problems for gas dynamics without Riemann problem solvers](#), *Numer. Methods Partial Differential Equations* 18 (5) (2002) 584–608. doi:10.1002/num.10025. URL <https://doi.org/10.1002/num.10025>
- [29] B. Fornberg, N. Flyer, [Fast generation of 2-D node distributions for mesh-free PDE discretizations](#), *Comput. Math. Appl.* 69 (7) (2015) 531–544. doi:10.1016/j.camwa.2015.01.009. URL <https://doi.org/10.1016/j.camwa.2015.01.009>
- [30] C. Geuzaine, J.-F. Remacle, [Gmsh: A 3-D finite element mesh generator with built-in pre- and post-processing facilities](#), *Internat. J. Numer. Methods Engrg.* 79 (11) (2009) 1309–1331. doi:10.1002/nme.2579. URL <https://doi.org/10.1002/nme.2579>

- [31] P.-O. Persson, G. Strang, [A simple mesh generator in Matlab](#), SIAM Rev. 46 (2) (2004) 329–345. doi:[10.1137/S0036144503429121](#).
URL <https://doi.org/10.1137/S0036144503429121>
- [32] I. Tominec, P.-F. Villard, E. Larsson, V. Bayona, N. Cacciani, An unfitted radial basis function generated finite difference method applied to thoracic diaphragm simulations (2021). arXiv:[2103.03673](#).
- [33] I. Tominec, E. Breznik, [An unfitted RBF-FD method in a least-squares setting for elliptic PDEs on complex geometries](#), J. Comput. Phys. 436 (2021) Paper No. 110283, 24. doi:[10.1016/j.jcp.2021.110283](#).
URL <https://doi.org/10.1016/j.jcp.2021.110283>
- [34] G. A. Barnett, A Robust RBF-FD Formulation based on Polyharmonic Splines and Polynomials, Ph.D. thesis, University of Colorado at Boulder, Dept. of Applied Mathematics, Boulder, CO, USA (2015).
- [35] N. Flyer, B. Fornberg, V. Bayona, G. A. Barnett, On the role of polynomials in RBF-FD approximations: I. Interpolation and accuracy, J. Comput. Phys. 321 (2016) 21–38. doi:[10.1016/j.jcp.2016.05.026](#).
- [36] V. Bayona, N. Flyer, B. Fornberg, G. A. Barnett, On the role of polynomials in RBF-FD approximations: II. Numerical solution of elliptic PDEs, J. Comput. Phys. 332 (2017) 257–273. doi:[10.1016/j.jcp.2016.12.008](#).
- [37] V. Bayona, An insight into RBF-FD approximations augmented with polynomials, Comput. Math. Appl. 77 (2019) 2337–2353. doi:[/10.1016/j.camwa.2018.12.029](#).
- [38] M. Jančić, J. Slak, G. Kosec, [Monomial augmentation guidelines for RBF-FD from accuracy versus computational time perspective](#), J. Sci. Comput. 87 (1) (2021) Paper No. 9, 18. doi:[10.1007/s10915-020-01401-y](#).
URL <https://doi.org/10.1007/s10915-020-01401-y>
- [39] I. Tominec, Rectangular and square RBF-FD matrices in MATLAB, <https://github.com/IgorTo/rbf-fd> (2021). doi:[10.5281/zenodo.4525550](#).
- [40] M. Nazarov, A. Larcher, [Numerical investigation of a viscous regularization of the Euler equations by entropy viscosity](#), Comput. Methods Appl. Mech. Engrg. 317 (2017) 128–152. doi:[10.1016/j.cma.2016.12.010](#).
URL <https://doi.org/10.1016/j.cma.2016.12.010>
- [41] A. Kurganov, G. Petrova, B. Popov, [Adaptive semidiscrete central-upwind schemes for non-convex hyperbolic conservation laws](#), SIAM J. Sci. Comput. 29 (6) (2007) 2381–2401. doi:[10.1137/040614189](#).
URL <https://doi.org/10.1137/040614189>
- [42] R. Liska, B. Wendroff, [Comparison of several difference schemes on 1D and 2D test problems for the Euler equations](#), SIAM J. Sci. Comput. 25 (3) (2003) 995–1017. doi:[10.1137/S1064827502402120](#).
URL <https://doi.org/10.1137/S1064827502402120>
- [43] I. Tominec, M. Nazarov, E. Larsson, Stability estimates for the rbf methods applied to time-dependent hyperbolic pdes (to appear) (2021).